

## Rupture modes in laboratory earthquakes: Effect of fault prestress and nucleation conditions

Xiao Lu,<sup>1</sup> Ares J. Rosakis,<sup>1</sup> and Nadia Lapusta<sup>2</sup>

Received 9 September 2009; revised 25 May 2010; accepted 6 August 2010; published 1 December 2010.

[1] Seismic inversions show that earthquake risetimes may be much shorter than the overall rupture duration, indicating that earthquakes may propagate as self-healing, pulse-like ruptures. Several mechanisms for producing pulse-like ruptures have been proposed, including velocity-weakening friction, interaction of dynamic rupture with fault geometry and local heterogeneity, and effect of bimaterial contrast. We present experimental results on rupture mode selection in laboratory earthquakes occurring on frictional interfaces, which were prestressed both in compression and in shear. Our experiments demonstrate that pulse-like ruptures can exist in the absence of a bimaterial effect or of local heterogeneities. We find a systematic variation from crack-like to pulse-like rupture modes with both (1) decreasing nondimensional shear prestress and (2) decreasing absolute levels of shear and normal prestress for the same value of nondimensional shear prestress. Both pulse-like and crack-like ruptures can propagate with either sub-Rayleigh or supershear rupture speeds. Our experimental results are consistent with theories of ruptures on velocity-weakening interfaces, implying that velocity-weakening friction plays an important role in governing the dynamic behavior of earthquake ruptures. We show that there is no measurable fault-normal stress decrease on the fault plane due to the nucleation procedure employed in experiments, and hence, this is not a factor in the rupture mode selection. We find that pulse-like ruptures correspond to the levels of nondimensional shear prestress significantly lower than the static friction coefficient, suggesting that faults hosting pulse-like ruptures may operate at low levels of prestress compared to their static strength.

**Citation:** Lu, X., A. J. Rosakis, and N. Lapusta (2010), Rupture modes in laboratory earthquakes: Effect of fault prestress and nucleation conditions, *J. Geophys. Res.*, 115, B12302, doi:10.1029/2009JB006833.

### 1. Introduction

[2] One of the central questions in rupture dynamics is what controls the duration of slip at a point on a rupturing fault. Such duration is often called the risetime. If the risetime is significantly shorter than the overall duration of a seismic event, the rupture is called pulse-like. Otherwise it is called crack-like. In the crack-like rupture mode, the risetime is comparable to the overall rupture duration. Early analytical and numerical studies concentrated on the analysis of crack-like shear ruptures, due to the theoretical analogy with opening cracks and the fact that rupture models with uniform interfaces governed by linear slip-weakening friction produce crack-like rupture propagation [Kostrov, 1966; Ida, 1972; Andrews, 1976; Madariaga, 1976]. At the same time, seismic inversions of large events have typically produced risetimes

that are several times smaller than the overall rupture duration [e.g., Kanamori and Anderson, 1975], pointing to the existence of pulse-like ruptures during natural earthquakes. The shorter durations were later attributed to the arrest waves from the finite fault width which is several times smaller than the rupture length for large events [Day, 1982; Johnson, 1992]. In such models, the risetime is related to the width of the fault. However, the work of Heaton [1990] presented inversions with earthquake risetimes significantly shorter than what would be predicted based on fault widths, arguing that earthquakes propagate as self-healing pulses and advocating velocity-weakening friction as the cause of such behavior.

[3] Since the influential work of Heaton [1990], many theoretical studies have been devoted to understanding the underlying physics of pulse-like sliding. Pulse-like ruptures have been obtained in a number of numerical simulations that include significant weakening of interface friction with sliding velocity [Cochard and Madariaga, 1994; Perrin et al., 1995; Beeler and Tullis, 1996; Cochard and Madariaga, 1996; Zheng and Rice, 1998; Nielsen et al., 2000; Lapusta and Rice, 2004; Shi et al., 2008; Noda et al., 2009]. The use of such friction laws in numerical studies have been supported by recent rock experiments and theoretical studies that have

<sup>1</sup>Graduate Aerospace Laboratories, California Institute of Technology, Pasadena, California, USA.

<sup>2</sup>Division of Engineering and Applied Science and Division of Geological and Planetary Sciences, California Institute of Technology, Pasadena, California, USA.

uncovered strongly velocity-weakening friction at seismic slip velocities [Tsutsumi and Shimamoto, 1997; Tullis and Goldsby, 2003; Di Toro et al., 2004; Rice, 2006; Yuan and Prakash, 2008a, 2008b]. Other explanations for the occurrence of pulse-like ruptures have also been proposed, including interaction of ruptures with local heterogeneities [Beroza and Mikumo, 1996; Olsen et al., 1997; Day et al., 1998] and normal stress variation due to difference in material properties across the interface or the so-called “bimaterial effect” [Andrews and Ben-Zion, 1997; Cochard and Rice, 2000; Ben-Zion, 2001]. Recent studies [Festa and Vilotte, 2006; Shi and Ben-Zion, 2006; Liu and Lapusta, 2008; Shi et al., 2008; Lu et al., 2009] have shown that the dynamic rupture initiation procedure (rupture nucleation) can affect the characteristics of propagating rupture, including the rupture mode. Identifying which of the above mechanisms is the one responsible for producing short-duration pulse-like ruptures in natural earthquakes remains an open research question. At the same time, theoretical studies have shown that the selection of rupture modes is intimately related to the detailed nature of fault constitutive laws as well as to the stress conditions on the faults, and has important implications for energy partition and heat generation during earthquakes, scaling laws, and spatio-temporal complexity of fault slip [Heaton, 1990; Cochard and Madariaga, 1994; Perrin et al., 1995; Beeler and Tullis, 1996; Cochard and Madariaga, 1996; Zheng and Rice, 1998; Nielsen et al., 2000; Ben-Zion, 2001; Nielsen and Madariaga, 2003; Lapusta and Rice, 2004; Lu et al., 2007; Shi et al., 2008; Noda et al., 2009].

[4] In the current study, we present results of laboratory experiments which mimic natural earthquakes and allow us to directly observe risetimes and hence the resulting rupture modes. The experimental design, based on the work of Xia et al. [2004], incorporates a preexisting fault interface with a controlled prestress both in compression and in shear, a nucleation mechanism which initiates dynamic rupture under a uniform and known level of prestress, and experimental diagnostics [Lykourafitis et al., 2006b] which allows us to capture the details of dynamic rupture propagation and, in particular, to conclusively determine the risetime and rupture speed. We have developed a treatment procedure for the sliding surfaces that ensures that nominally the same frictional properties prevail in all samples. The experimental setup (described in detail in the review by Rosakis et al. [2007]) is essentially 2-D, which enables comparison with a number of theoretical studies. The experimental procedure, sample preparation, experimental measurements, and their interpretation are briefly summarized in sections 2–3. In particular, section 3.3 investigates the effect of the thickness of the plate used in the experiments on the resulting rupture propagation behavior.

[5] Since our experiments contain no heterogeneities in interface properties or in the applied prestress nor do they feature any bimaterial contrast, any pulse-like ruptures appearing in the experiments would have to be due to either the velocity dependence of friction or the nucleation procedure. An initial set of pilot experiments [Lu et al., 2007] has already demonstrated the existence of pulse-like ruptures in this experimental setup. Moreover, the study of Lu et al. [2007] discovered a systematic variation of rupture mode from crack-like to pulse-like as the nondimensional ratio of shear prestress to normal prestress, or “nondimensional prestress,” was increased. They also showed that the

experimental results are consistent with the theoretical predictions of Zheng and Rice [1998] for faults governed by velocity-weakening friction. Lu et al. [2007] also pointed out that (1) the results of Zheng and Rice [1998] additionally predict that the rupture mode should change as the absolute level of normal and shear prestress is varied, for the same nondimensional prestress and (2) the role of the nucleation procedure needs to be further investigated. The experimental nucleation procedure involves an explosion of a small (<0.1 mm) wire that leads to local reduction of the compressive normal stress and allows the shear prestress to initiate the rupture. If such normal stress reduction were to propagate along the interface with elastodynamic waves, reducing frictional resistance, it could itself be a factor in the rupture mode selection.

[6] Motivated by the observations of the pilot study of Lu et al. [2007], we significantly extend it to consider the effect of the absolute level of prestress (section 4) as well as the experimental nucleation procedure (section 6). We show that rupture modes exhibit a systematic variation from pulse-like to crack-like as the absolute level of prestress is increased, a finding consistent with the theory of Zheng and Rice [1998] for velocity-weakening interfaces. As a bonus, the preliminary results of Lu et al. [2007] on the systematic mode variation due to nondimensional prestress are confirmed for a wider range of experimental parameters. To determine the potential effect of the nucleation procedure, we (1) conduct experiments with different intensity of the nucleating explosion and (2) we measure relative fault-normal particle velocities to estimate the potential normal stress changes induced by the nucleation procedure further along the interface. The findings presented in section 6 indicate that these aspects of the nucleation procedure have no effect on the rupture mode selection.

[7] The present study also features an extensive investigation of rupture speeds (sections 7–8). Lu et al. [2007] have shown that both pulse-like and crack-like modes can transition to supershear rupture speeds, with the difference in speeds between the pulse-like and crack-like modes that is consistent with the theoretical study of rupture speeds on velocity-weakening interfaces by Samudrala et al. [2002]. The estimate for rupture speeds is confirmed in this work by a detailed computation of the rupture speed evolution for pulse-like and crack-like ruptures. The combined map for experimental conditions that lead to pulse-like versus crack-like modes and sub-Rayleigh versus supershear rupture speeds is then presented and analyzed. All four potential rupture types, sub-Rayleigh pulse-like, supershear pulse-like, sub-Rayleigh crack-like, and supershear crack-like, are observed in our experiments. Sub-Rayleigh pulse-like modes correspond to the lowest prestress levels studied.

[8] If pulse-like ruptures prevail on natural faults, at least for large earthquakes, our study provides further support for the importance of velocity-weakening friction for dynamics of natural earthquakes and implies that major faults operate at low levels of prestress. Our conclusions are summarized in section 9.

## 2. Experimental Design

### 2.1. Configuration That Mimics Crustal Earthquakes

[9] Our experimental setup mimics a fault in the Earth’s crust that is prestressed both in compression and in shear

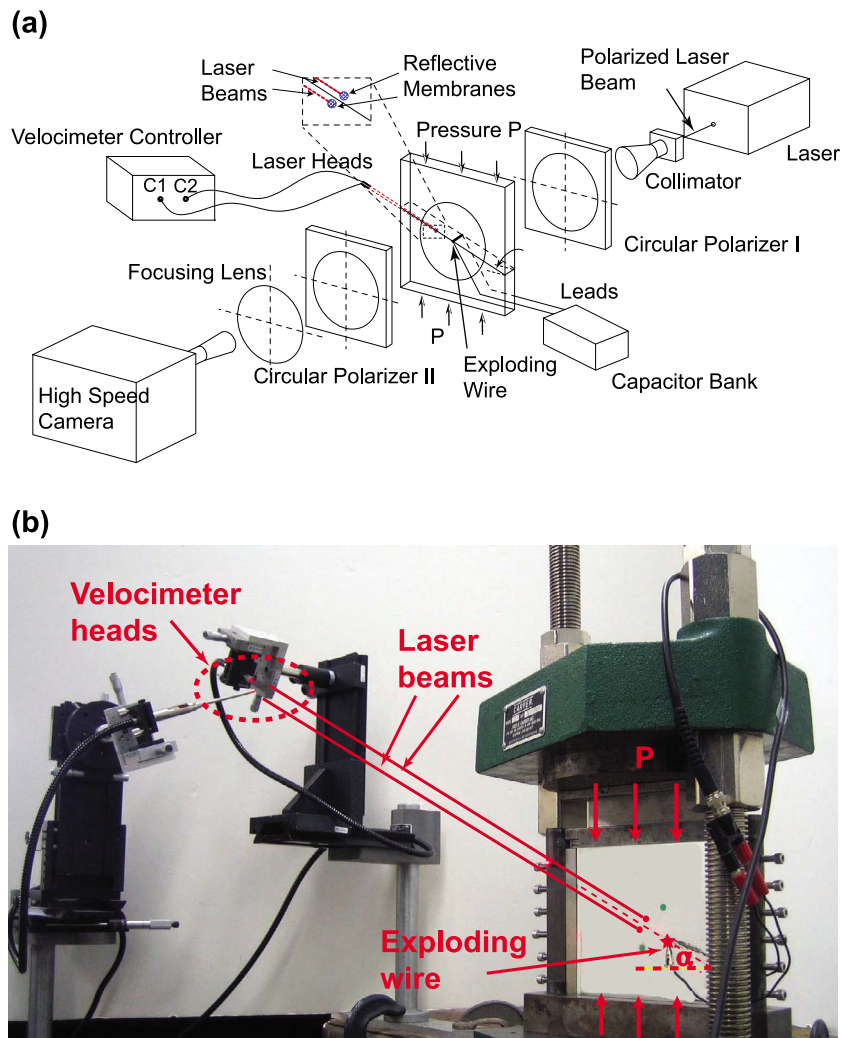


**Figure 1.** (a) Schematic illustration of the experimental configuration. Homalite samples are cut with an inclination angle  $\alpha$  and compressed with the far-field load  $P$ . Dynamic photoelasticity and laser velocimetry are used to capture the full field information of rupture propagation as well as the local sliding velocity of the interface. Rupture nucleation is achieved by a local pressure release due to an explosion of a thin wire. (b) A photograph of the experimental setup.

[Xia *et al.*, 2004; Lu *et al.*, 2007; Rosakis *et al.*, 2007]. A square Homalite plate (Figure 1a), with the dimensions  $150 \text{ mm} \times 150 \text{ mm} \times 10 \text{ mm}$ , is cut into two identical quadrilaterals, introducing a fault plane with an inclination angle  $\alpha$  with respect to one set of the plate edges. Unidirectional compression  $P$  is applied to the top and bottom edges. The fault surfaces are treated to create the same texture and hence the same friction properties in all specimens, as described in section 2.3. Experimental parameters  $P$  and  $\alpha$  determine the resolved shear traction  $\tau_0 = P \sin \alpha \cos \alpha$  and normal traction  $\sigma_0 = P \cos^2 \alpha$  on the fault. The nondimensional shear prestress  $f_0 = \tau_0 / \sigma_0 = \tan \alpha$  indicates how close the interface is to failure according to the Coulomb criterion. Because the static friction coefficient of the interface is about 0.6, the inclination angle  $\alpha$  is chosen to be  $30^\circ$  or smaller to ensure that sliding does not occur during the static preloading stage. By varying  $\alpha$ , we can consider the effect of different levels of nondimensional fault prestress on rupture dynamics. Varying  $P$  allows us to study the effect of the absolute prestress level.

[10] Dynamic rupture is initiated in the middle of the plate and captured using high-resolution dynamic photoelasticity and laser velocimetry [Lykotrafitis *et al.*, 2006b, 2006c; Rosakis *et al.*, 2007]. The rupture is triggered simultaneously across the entire thickness of the plate using an explosion of a thin wire as described in section 2.2. As the result, the rupture is dominated by 2-D in-plane slip, similarly to large strike-slip earthquakes that saturate the entire seismogenic depth. The bilaterally spreading rupture is observed only until reflected waves return from the edges of the plate, to avoid interaction between the rupture and the specimen boundaries. A typical observation window is  $65 \mu\text{s}$ .

[11] Elastic properties of the bulk material, Homalite, are as follows [Dally and Riley, 1991]: Young's modulus  $E = 3.86 \text{ GPa}$ , shear modulus  $\mu = 1.43 \text{ GPa}$ , Poisson's ratio  $\nu = 0.35$ , density  $\rho = 1200 \text{ kg/m}^3$ . The dynamic wave speeds of Homalite are measured by ultrasonic transducers operating at  $5 \text{ MHz}$  [Lykotrafitis, 2006a]: shear wave speed  $C_s = 1249 \text{ m/s}$ , longitudinal wave speed  $C_p = 2187 \text{ m/s}$ , and Rayleigh wave speed  $C_R = 1155 \text{ m/s}$ . Homalite has about

20 times smaller shear modulus than typical rock materials. Since estimates of critical crack sizes and nucleation sizes are proportional to shear modulus, smaller shear modulus for Homalite translates into smaller critical length scales, assuming similar friction properties for rocks and Homalite. This enables us to reproduce rupture phenomena in much smaller samples than would be needed for experiments conducted in rocks.

## 2.2. Mechanism of Rupture Nucleation

[12] Initiation of dynamic rupture is achieved by an explosion of a thin wire. A nickel wire with a diameter of 0.08 mm is embedded within a 0.1 mm hole across the entire plate thickness. The ends of the wire are connected to a charged capacitor. By abrupt discharge, the stored electric energy is released and the surge of the current turns the wire into plasma [Rosakis *et al.*, 2007]. The explosion relieves fault-normal compression locally, decreasing friction and allowing shear rupture to start under the action of the resolved shear stress in a region around the explosion site. Afterward, dynamic rupture propagates spontaneously outside the nucleation region, since (1) rupture concentrates shear stress at its tips, matching static friction outside the area affected by the explosion and spreading farther, and (2) fault locations behind the rupture front experience dynamic reduction in friction strength, as would be expected from either slip-weakening or velocity-weakening friction.

[13] The nucleation mechanism of the wire explosion has a number of experimental advantages. The electric signal that causes the explosion enables synchronization of multiple diagnostic instruments. Rupture initiation is achieved with known and adjustable stress conditions outside of the nucleation region. This allows us to reproduce the same experimental conditions multiple times while taking different diagnostic measurements, such as velocimeter measurements at different locations.

[14] At the same time, the initiation procedure introduces additional complexity. It is different from the process of gradually accelerating slip occurring under slow stress increase due to tectonic loading obtained in a number of earthquakes models [e.g., Lapusta *et al.*, 2000]. However, it is conceptually representative of earthquake nucleation by rapid stress changes due to seismic waves. Numerical simulations of dynamic rupture have shown that details of rupture initiation can significantly affect the subsequent rupture propagation [Festa and Vilotte, 2006; Shi and Ben-Zion, 2006; Liu and Lapusta, 2008; Shi *et al.*, 2008; Lu *et al.*, 2009]. Hence it is important to understand the effect of the initiation procedure on dynamic rupture in our experiments. To that end, we conduct experiments with explosions of different strength and perform fault-normal velocity measurements outside the nucleation region, as discussed in section 6.

## 2.3. Surface Preparation for Specimens

[15] For meaningful comparison between different experiments and for experimental repeatability, it is critical for all specimens to have the same surface preparation and hence the same friction properties. We have developed a controlled surface preparation procedure. As shown in Figure 2a, the original surface obtained from machining has periodic cutting scratches. By polishing it with a diluted solution of Miromet polishing compound, we are able to

remove the scratches and make the surface transparent (Figure 2b). The next step is to use a bead blaster to roughen the polished surface. Fine glass beads of 44  $\mu\text{m}$  to 88  $\mu\text{m}$  in diameter are driven by compressed air out of the nozzle and strike the polished surface, creating the same surface texture in all samples (Figure 2c). Three-dimensional scanning by a surface profiler (Figure 2d) gives the average roughness of  $R_a = 4.5 \mu\text{m}$ . The average roughness is defined as the average height of the surface profile.

## 2.4. High-Resolution Diagnostics: Dynamic Photoelasticity and Laser Velocimetry

[16] As shear rupture grows bilaterally away from the nucleation region, high-speed photography, in conjunction with dynamic photoelasticity, is used to capture full-field images of the transient dynamic event. As shown in Figure 1a, collimated laser beams are used to illuminate the transparent specimen. A pair of circular polarizers, one in front of and one behind the Homalite specimen, creates a fringe pattern that represents contours of maximum shear stress. The shear stress in each fringe is given by the stress optical law,  $2\tau_{\text{max}} = \sigma_1 - \sigma_2 = NF_\sigma/h$ , where  $F_\sigma$  is the material's stress optical coefficient,  $h$  is the specimen thickness,  $\sigma_1$  and  $\sigma_2$  are the principal stresses, and  $N = n + 1/2$  (with  $n = 0, 1, 2, \dots$ ) is the isochromatic fringe order. A digital high-speed camera is positioned at the end of the optical axis to record a series of 16 photoelastic images with the programmable interframe time that can vary from 2 to 4  $\mu\text{s}$ .

[17] In addition to the full-field photoelastic images, we use two velocimeters based on laser interferometry to measure particle velocity histories of two points, one above and one below the fault interface (Figure 1b). Two reflective membranes are glued at the points of interest, and two separate laser beams are focused on the sides of the two membranes to record either the fault-parallel or fault-normal particle velocity. The size of the each laser beams is 66  $\mu\text{m}$  and the distance between the two measurements is about 500  $\mu\text{m}$ . The difference between the two measured fault-parallel particle velocities represents the interface sliding velocity plus elastic deformation between the two measurement points [Rosakis *et al.*, 2007]. As discussed in section 3.2, the elastic deformation is taken into account when the onset and healing of the interfacial sliding is determined. The maximum frequency response of the velocimeters is 1.5 MHz, which is fast enough to track rapid particle velocity changes during dynamic rupture. The velocimeters can measure particle velocity of up to 10 m/s, enabling us to record high slip velocity at rupture fronts. The signal-to-noise ratio of the velocimeters is 86 dB. The resolution is  $2.5 \mu\text{m s}^{-1}/\sqrt{\text{Hz}}$ , which is frequency dependent. For a typical measurement in our study with the frequency of 1 MHz and velocity amplitude of 1 m/s, the resolution is 2.5 mm/s.

## 3. Experimental Measurements and Their Interpretation

### 3.1. Measurements of Particle Velocity and Full-Field Photoelastic Snapshots

[18] Let us use representative experimental results to illustrate the two diagnostic methods (Figure 3). In these experiments, the inclination angle is  $\alpha = 30^\circ$  and the externally applied compression is  $P = 14 \text{ MPa}$ . Particle

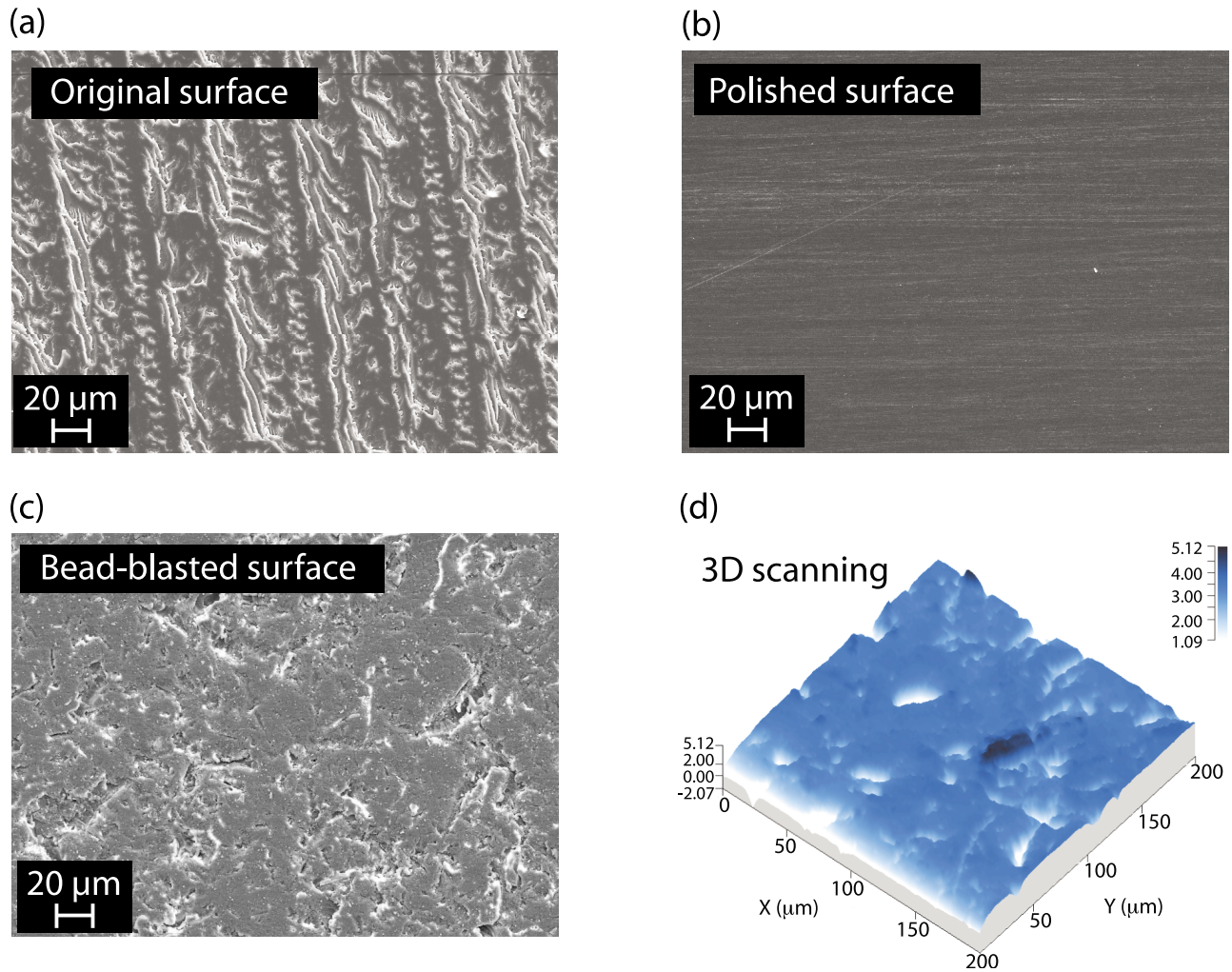


**Figure 2.** Preparation of surfaces that form frictionally held interfaces. (a) SEM (scanning electron microscopy) image of the specimen surface after cutting, showing periodic scratches. (b) SEM image of the polished surface of the specimen. (c) SEM image of the surface roughened by bead blasting. (d) Three-dimensional scanning image of the prepared sliding surface by a surface profiler.

velocity measurements at the location of 20 mm from the hypocenter are shown in Figure 3a. Individual channels marked as “upper” and “lower” correspond to particle velocity histories of points above and below the interface, respectively; the plotted measurements are shifted by  $-3$  m/s for clarity. The particle velocities are approximately anti-symmetric, as would be expected for shear rupture. The oscillatory nature of the traces and deviations from anti-symmetry are discussed in section 3.3. The points on the two sides of the interface start to move shortly after  $10 \mu\text{s}$  when the  $P$  wave arrives. They move together initially, and then, at about  $15 \mu\text{s}$ , they exhibit relative motion. The particle velocities at the arrival of the  $P$  wave, before the start of the relative motion, may be exaggerated due to the oscillatory nature of the particle velocity trace potentially caused by the 3-D effect in our experiments, as discussed further in section 3.3. The subsequent relative motion is the sum of the elastic deformation between the two points and relative sliding, or slip, on the interface. Relative velocity between the two measurement points is computed by subtracting the velocity history of the point below the interface

from that above the interface. The green dot indicates our estimate of rupture arrival time or the initiation of relative sliding. Criteria for determining rupture arrival and interface locking are discussed in section 3.2. The relative velocity reaches the maximum of about 4.5 m/s and it is of the order of 1 m/s throughout the observation window. This means that the interface does not lock during the observation window, indicating what we define to be a crack-like mode. The timing of the shear wave arrival, indicated by a vertical dashed line on the relative velocity trace, provides us with a conclusive way of judging whether rupture is supershear or not. In Figure 3a, it is apparent that the rupture is supershear, as it arrives sooner than the shear wave.

[19] To get the slip velocity profile farther along the interface, at the location of 40 mm, another experiment is done under the same experimental conditions (Figure 3c). In this case, the  $P$  wave arrival induces a smaller symmetric motion of the points above and below the interface. This is consistent with both the decrease of the 3-D effect and the decaying amplitude of the  $P$  wave farther from the hypocenter. The initiation of sliding occurs at  $27.8 \mu\text{s}$  and con-

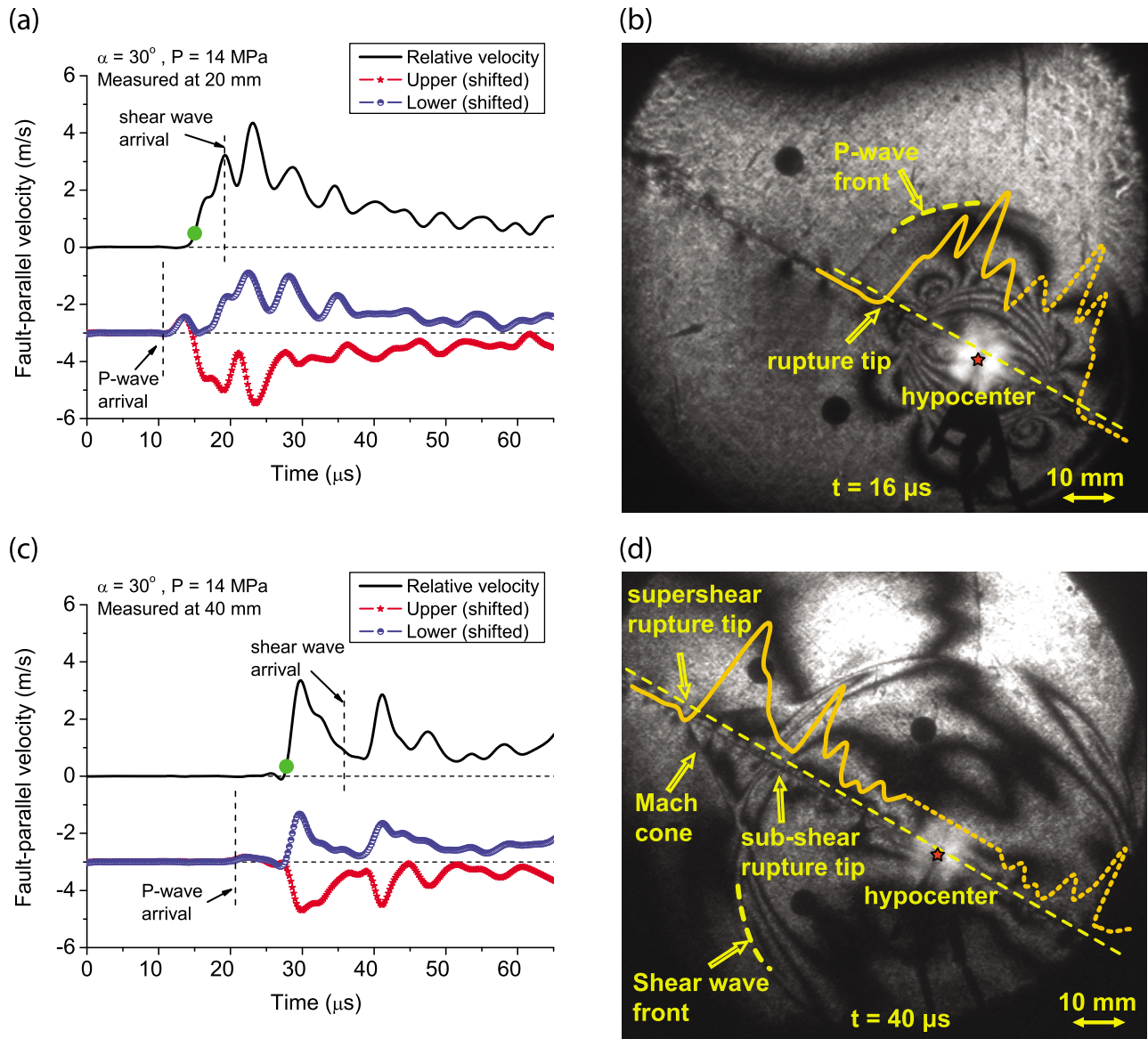


**Figure 3.** Illustration of the experimental diagnostics for an experiment with the inclination angle  $\alpha = 30^\circ$  and compressive load  $P = 14$  MPa. (a and c) Fault-parallel velocity histories measured 20 and 40 mm from the rupture nucleation site, respectively. The velocities of the upper and lower measurement points are shifted by 3 m/s.  $P$  wave and shear wave arrivals are indicated by dashed lines. The estimated rupture initiation time is marked by a green dot. Once initiated, the sliding continues throughout the observation window, corresponding to the crack-like rupture mode. The rupture is supershear, since rupture initiation occurs earlier than the shear wave arrival time. (b and d) Dynamic photoelastic images captured 16 and 40  $\mu\text{s}$  after the rupture nucleation, respectively. Fringes represent contours of maximum shear stress. The relative velocity profiles from Figures 3a and 3c are superimposed on the photoelastic images, with the straight dashed yellow line indicating the relative velocity corresponding to the green dots in Figures 3a and 3c.

tinues throughout the observation window, indicating that the rupture remains crack-like. The rupture front is farther ahead with respect to the shear wave arrival than in Figure 3a, confirming supershear propagation.

[20] In order to further analyze the experiment, the relative velocity record is superimposed on the photoelastic fringe map (Figures 3b and 3d). This superposition, done for visualization purposes, illustrates stress concentrations at rupture tips and converts time-dependent rupture history at

one location into an approximation of the space-dependent rupture profile at the time of the photoelastic snapshot. Converting the time history of the sliding velocity into spatial variation along the fault is based on the assumption of a constant rupture speed. Since rupture is expected to be equibilateral, a mirrored profile (with respect to the nucleation site) is added for visualization purposes. The hypocenter is marked by a star. The circular  $P$  wave and shear wavefronts are marked with dashed lines. Figures 3b and 3d

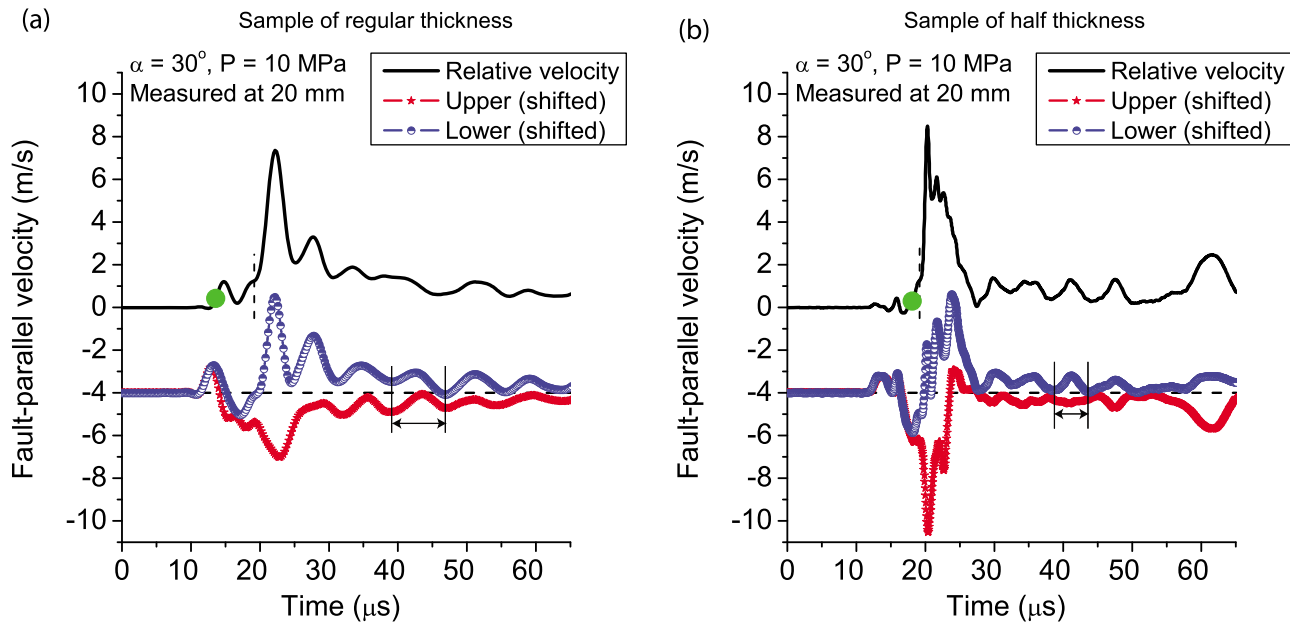


**Figure 4.** Comparison of fault-parallel velocity measurements between (a) a regular sample of 10 mm thickness and (b) a twice thinner sample of 5 mm thickness. For both cases, the inclination angle is  $\alpha = 30^\circ$ , the compressive load is  $P = 10$  MPa, and the measurement location is 20 mm. The wavelengths of oscillations in the slip velocity profile become about twice smaller for the twice thinner samples, indicating that the oscillations are at least partially due to the 3-D effect.

give the superposition of photoelastic fringe patterns and relative sliding velocity for the times of 16  $\mu$ s and 40  $\mu$ s, respectively, illustrating the progression of the rupture along the interface. At the time of 40  $\mu$ s, the supershear rupture is well developed and two Mach lines are emitted from the supershear rupture tip (Figure 3d). The set of 16 photoelastic images allows us to compute the evolution of rupture speed as the rupture propagates along the interface as discussed in section 7.1. The combined diagnostics of laser velocimetry and dynamic photoelasticity enables us to conclusively determine both the risetime (or local rupture duration) and the rupture speed.

### 3.2. Criteria for Determining Rupture Initiation and Locking Times

[21] In order to consistently identify the timing of both interfacial sliding initiation and interfacial locking (or healing), and thus to determine the rupture duration, criteria are established which account for the elastodynamic shear deformation between the measurement points [Lu *et al.*, 2007]. Interfacial sliding starts if and only if shear stress  $\tau$  on the interface is equal to the static friction strength of the interface which, in turn, is equal to normal stress  $\sigma$  times the static friction coefficient  $f_s$ . As discussed in section 6.1, normal stress  $\sigma$  at the measurement locations is approximately equal to the initial normal stress  $\sigma_0$ . The difference between the static friction resistance  $f_s\sigma_0$  and initial shear stress  $\tau_0$  at a point along the interface is overcome by the dynamic shear stress increase arriving with either the rupture tip or the shear wavefront. Assuming uniform shear stress between the two measurement points, this difference in shear stress can be converted into a critical relative displacement  $\delta_c$  that can be sustained between the two mea-

surement points before interfacial sliding initiates. If  $\mu$  is the shear modulus of Homalite-100 and  $D$  is the distance between the two measurement location, the critical displacement is given by:

$$\delta_c = D \frac{(f_s\sigma_0 - \tau_0)}{\mu} = D \frac{P \cos^2 \alpha (f_s - f_0)}{\mu}. \quad (1)$$

[22] The time of rupture initiation can be established by integrating the relative velocity records and determining the time at which the displacement equal to  $\delta_c$  is accumulated; this time is marked by green filled dots in Figure 3. This time also corresponds to a particular value  $\delta_c$  of the relative velocity which we call the elastic cutoff velocity. For the experimental conditions of Figure 3, the critical displacement  $\delta_c$  is calculated to be 0.08  $\mu$ m and the elastic cutoff velocity is  $\delta_c = 0.43$  m/s. That value of relative velocity is plotted as the yellow dotted interface-parallel line in Figures 3b and 3d.

[23] To determine when the sliding stops, we employ two criteria. According to the first criterion, sliding stops when the relative velocity becomes smaller than the elastic cutoff value  $\delta_c$ . If the relative velocity decreases below  $\delta_c$  several times, we take the last time as the time of interface locking. Those times are marked by half-filled red dots that show ruptures with slip arresting within the time window of observation. The second, more conservative, criterion is to insist that the relative velocity drops to zero and that the integral of relative velocity from that time until the end of observation time is a small fraction (less than 5%) of the total accumulated relative displacement. The corresponding times are marked by fully filled red dots. The two different locking criteria produce the same qualitative results with

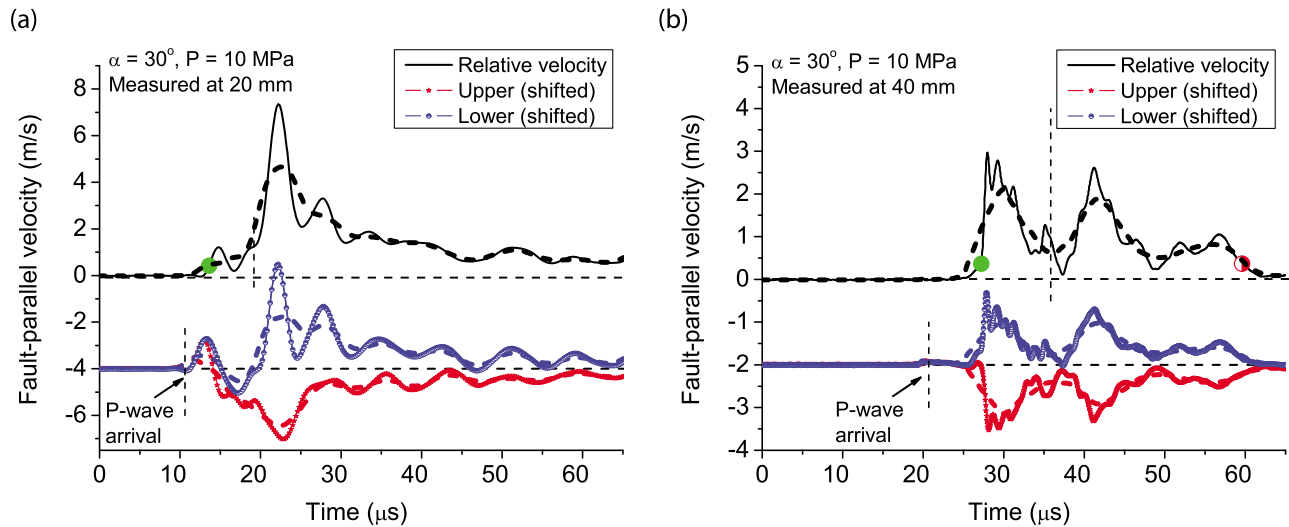


**Figure 5.** Evaluation of deviations from antisymmetry of the fault-parallel velocity on the two sides of the interface measured at (a) 20 mm and (b) 40 mm from the nucleation region. For both measurements,  $\alpha = 30^\circ$  and  $P = 10$  MPa. Dashed lines are smoothed velocity profiles that are constructed by averaging the measurement within the window of  $5 \mu\text{s}$ , in an attempt to approximately remove the 3-D effect. Deviations from asymmetry in the upper and lower measurements are present at 20 mm but virtually disappear at 40 mm. Smoothing the velocity profiles decreases the asymmetry, indicating that it is at least partially due to the 3-D effect.

respect to rupture duration and hence rupture mode identification, as discussed in the following sections. In Figure 3, the interface at the measurement locations slips throughout the observation window and neither of the locking criteria are met.

### 3.3. Three-Dimensional Effect of the Plate Thickness

[24] It is important to understand whether the experimental setup is well described by a 2-D plane-stress model, as intended by the experimental design and assumed in the analysis of *Xia et al.* [2004] and *Lu et al.* [2009]. The plate dimensions, 150 mm by 150 mm, are much larger than the plate thickness of 10 mm, implying that 2-D plane-stress approximation should be valid. In addition, the rupture initiation mechanism acts simultaneously through the thickness of the plate (section 2.2), further promoting the 2-D nature of the resulting stress and strain fields. At the same time, the fact that the stress and strain fields are nonuniform through the thickness of the plate may influence the experimental results; in the following, we refer to such potential influence as “the 3-D effect.” In particular, initial stages of rupture propagation over distances of the order of the plate thickness may be influenced by the locally 3-D geometry and that influence may persist at later times through wave-mediated stress transfers and interaction of those waves with the rupture propagation.

[25] To study the 3-D effect, we consider dynamic rupture in specimens of different plate thickness. Figure 4 compares two representative experiments conducted under the same experimental conditions but with plates of different thickness: 10 mm in Figure 4a and 5 mm in Figure 4b. Overall, the two experiments produce similar dynamic ruptures. In both cases, the peak slip velocity is around 8 m/s, there is no rupture arrest within the time window of observation, and the rupture is in the process of transitioning to supershear

speeds. One notable difference is in periods of velocity oscillations that are superimposed on the overall rupture profile. These periods are about twice smaller for the twice thinner specimen, as illustrated in Figure 4 by marking one period of the oscillations in the tail of the rupture profile. Note that the period of oscillations changes with time, being shorter at the rupture front and increasing farther along the rupture profile.

[26] Hence the 3-D effect does not change the main characteristics of dynamic ruptures but it does cause at least some of the observed oscillations in the measured particle velocity. This is likely due to waves bouncing between the lateral free surfaces. One consequence of this finding is that the 3-D effect needs to be removed from the measured velocity profiles before the profiles can be quantitatively compared with results of 2-D modeling. Note that the contribution of the 3-D effect to the upper and lower measurements is not exactly symmetric, as the computed relative velocity retains some oscillations. The lack of symmetry for the 3-D effect is likely due to the combination of the following factors: (1) the wire is embedded in a semicircular hole in the lower half of the plate, potentially creating some asymmetry in the radiated wavefields, (2) in most experiments, a small tensile crack is created in the lower half of the plate after the explosion, and (3) the measurements are sensitive to small differences in the alignment of the laser beams of the two velocimeters and in the position of the laser beams with respect to the interface.

[27] The 3-D effect could be partially or fully responsible for deviations from antisymmetric sliding observed in our experiments. In 2-D in-plane shear problems, the fault-parallel particle velocities are expected to be purely antisymmetric. Our experiments exhibit small deviations from antisymmetry for locations close to the nucleation region. Figure 5 shows velocity measurements at 20 mm and 40 mm

from the hypocenter. The measurements were made during two experiments with nominally the same experimental conditions. At the distance of 20 mm (Figure 5a), the lower and upper traces have opposite signs for most of the time but they are not exactly antisymmetric; for example, the lower measurement (blue line) has higher peak velocity than the upper measurement. When each of the two measurements is averaged using a  $5 \mu\text{s}$  time window, to partially remove the effect of the oscillations, the deviation from antisymmetry becomes less pronounced (dashed lines in Figure 5a), indicating that oscillations due to the 3-D effect are at least a contributing factor. Another factor that could contribute to breaking the antisymmetry is the wire explosion and, in particular, the potential Mode I component that it could create at the measurement location. Our measurements of fault-normal particle velocities (section 6.1) show that relative fault-normal motion is rather small and within the measurement error. Note that deviations from antisymmetry virtually disappear for the measurements farther along the interface, at 40 mm from the hypocenter (Figure 5b), as would be consistent with the decaying influence of both the 3-D nature of the initial rupture propagation and the nucleation procedure away from the hypocenter.

[28] The 3-D effect could also be partially or fully responsible for the observed increase in particle velocities after the  $P$  wave arrival but before the onset of relative motion, marked by the green dot, at the location of 20 mm (Figures 4a and 5a). One interpretation of such increase would be the  $P$  waves released by the initiation procedure, suggesting that the initiation procedure has an observable effect on the particle motion at the 20 mm measurement location. However, a couple of observations point toward the 3-D effect as a more likely explanation. First, the increase is within the amplitude of the oscillations observed in the particle velocity traces. Second, and more importantly, a simple increase in particle velocities before relative motion (Figure 4a) transforms into oscillations back-and-forth for the experiments with the twice thinner plate (Figure 4b), suggesting that the particle motion before the onset of relative sliding is strongly influenced, and in particular could be much amplified, by the 3-D effect.

[29] Note that the peak relative velocity at 40 mm is reduced in comparison to that at 20 mm, which could be due to several factors. One of them is the supershear transition that started at about 20 mm and developed over the course of propagation between 20 mm and 40 mm. Such transition could reduce the peak velocities of the decaying mother-rupture (second peak) while the supershear daughter rupture may not have gathered steam yet. Another factor is the 3-D effect of the specimen thickness: it causes appreciable oscillations that may affect the particle velocities; we are in the process of studying this effect in 3-D models of the experimental setup. There is also a possibility of a bulk dissipating mechanism in Homalite (e.g., viscoelasticity).

### 3.4. Experimental Repeatability

[30] Dynamic rupture on frictional interfaces is a highly nonlinear process with complex wave-mediated effects. Even for nominally the same experimental conditions (the same compression  $P$ , inclination angle  $\alpha$ , surface preparation, capacitor discharge, etc.) differences may appear, accumulate, and interact throughout the process of dynamic rupture,

potentially leading to different outcomes. To ensure that the rupture properties that we would like to study, such as the risetime and the rupture speed, are robust for the experiments under nominally the same experimental conditions, we have repeated experiments for each considered compression  $P$  and inclination angle  $\alpha$  at least twice. Typically, velocimetry measurements have been recorded at 20 mm in one of the tests and at 40 mm in the other test. In several key cases, more than two experiments have been done, repeating measurements at either 20 mm or 40 mm or both. High-speed photoelastic images have been taken for most experiments. Comparing these measurements, we have concluded that both the risetime (i.e., the local rupture duration) and the rupture speed are quite repeatable.

[31] As an example, consider the case of  $\alpha = 30^\circ$  and  $P = 14 \text{ MPa}$  shown in Figure 3. Figure 6 illustrates the range of experimentally obtained results for these experimental conditions. Four experiments have been conducted. In two of them, the particle velocity measurements have been obtained at the location of 20 mm (Figure 6a). In the other ones, the particle measurements have been obtained at the location of 40 mm (Figure 6b). We see that, at both locations, the overall shape of the rupture is quite similar and corresponds to what we call a crack-like mode, as the relative motion continues throughout the observation window. The rupture speeds are also quite similar; for example, Figure 6b shows the same supershear arrival for both experiments.

[32] The only notable discrepancy in the four experiments is the difference between the peak velocities in the measurements at the location of 20 mm (Figure 6a). Note that much of the difference is attributable to the oscillations; averaging velocities to approximately remove the 3-D effect, as discussed in section 3.3, would result in much closer values. The comparison clearly shows that peak particle velocities cannot be reliably reproduced and/or captured. The most likely explanation is the interaction and accumulation of small differences in various experimental factors (wire explosion, statistical differences in surface preparation, small deviations from the interface planarity, etc.). Velocimeter response at such high particle velocities and high frequencies may also be a factor.

[33] Photoelastic measurements show a very similar fringe pattern for tests at nominally the same experimental conditions at the same time in the rupture development, further confirming experimental repeatability. This is illustrated in Figures 6c and 6d for the case of  $\alpha = 25^\circ$  and  $P = 14 \text{ MPa}$ . Overall, the repeatability of the rupture shape and the rupture speed is quite remarkable, given the dynamic nature of the process and the number of factors that can influence the resulting rupture.

## 4. Experimental Observations of Systematic Variation in Risetime With Fault Prestress

[34] We use the experimental methodology described in sections 2 and 3 to investigate the effect of prestress on the risetime, i.e., the local rupture duration. This study builds on the work of *Lu et al.* [2007] as discussed in section 1. A series of experiments has been conducted with the inclination angle  $\alpha$  ranging from  $20^\circ$  to  $30^\circ$  and the compressive load  $P$  varying from 10 MPa to 30 MPa. Larger values of

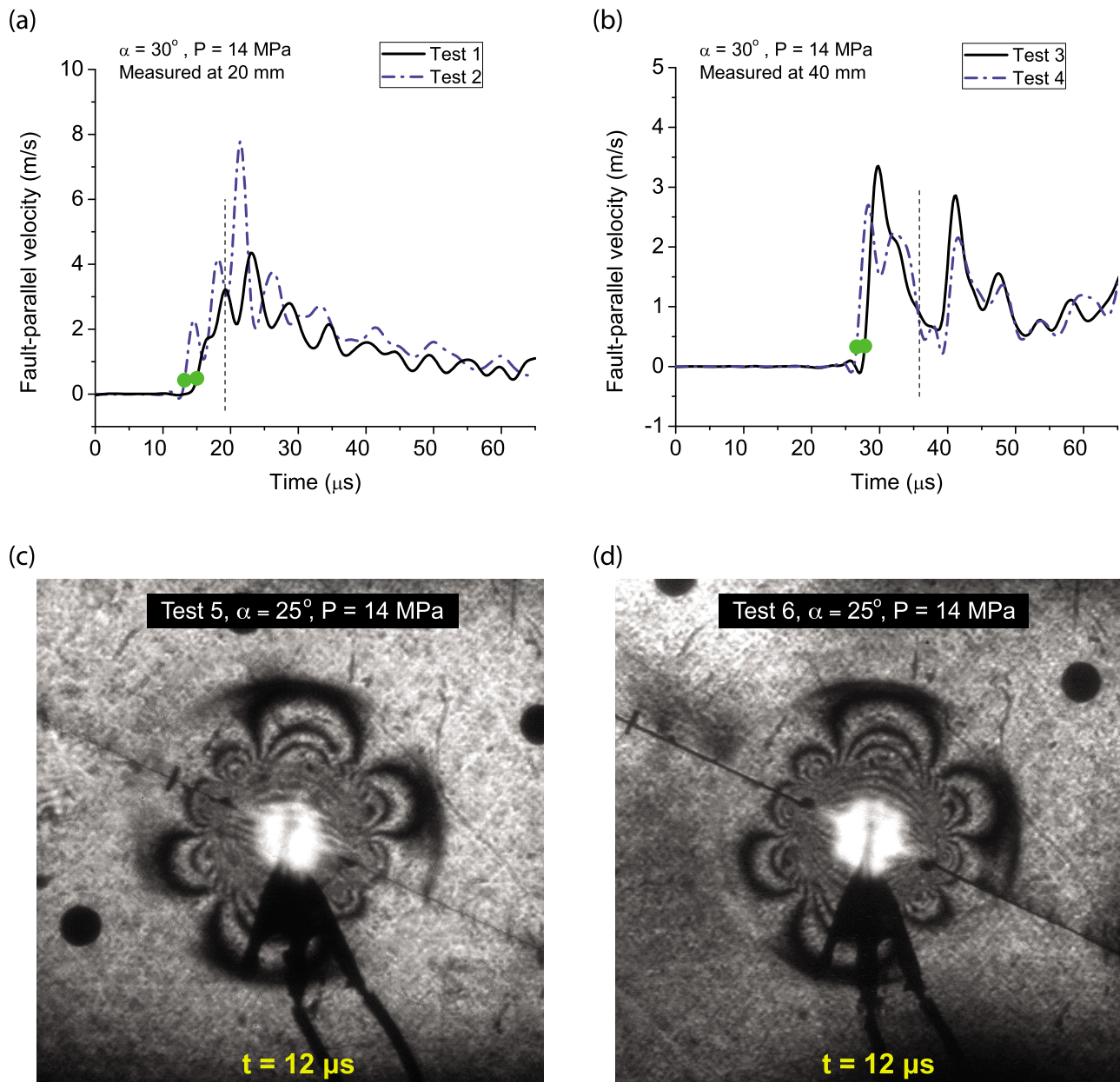


**Figure 6.** Illustration of the experimental repeatability. (a and b) Relative fault-parallel velocity measurements at the locations of 20 and 40 mm, respectively, using four experiments conducted with  $\alpha = 30^\circ$  and  $P = 14$  MPa. The overall velocity profile and rupture speeds match quite well between experiments done under nominally the same experimental conditions. The difference in peak velocity in Figure 6a is discussed in the text. (c and d) Photoelastic images captured shortly after the rupture initiation in two experiments with  $\alpha = 25^\circ$  and  $P = 14$  MPa show almost identical fringe patterns.

inclination angle  $\alpha$  result in higher levels of nondimensional shear prestress  $f_0 = \tau_0/\sigma_0 = \tan\alpha$ . Larger values of far-field compression  $P$  result in higher absolute levels of stress.

#### 4.1. Increase in Risetime With Nondimensional Shear Prestress

[35] We find that the risetime systematically increases as the inclination angle  $\alpha$  and hence the nondimensional shear prestress  $f_0 = \tau_0/\sigma_0 = \tan\alpha$  are increased. This systematic variation is shown in Figure 7 using relative fault-parallel velocity measurements for three inclination angles of  $20^\circ$ ,

$25^\circ$ , and  $30^\circ$ . Figures 7a–7c correspond to the compressive load  $P = 14$  MPa. The results for  $P = 10$  MPa, reported by Lu *et al.* [2007], are reproduced in Figures 7d–7f for comparison. Relative fault-parallel displacements for both compressive loads, obtained by numerical integration of the velocity profiles, are given in Figures 7g–7i. In all panels, rupture initiation and interface locking are marked by green and red dots, respectively, using the criteria described in section 3.2.

[36] For both values of  $P$  and for smaller inclination angles  $\alpha = 20^\circ$  and  $\alpha = 25^\circ$ , the resulting ruptures experience

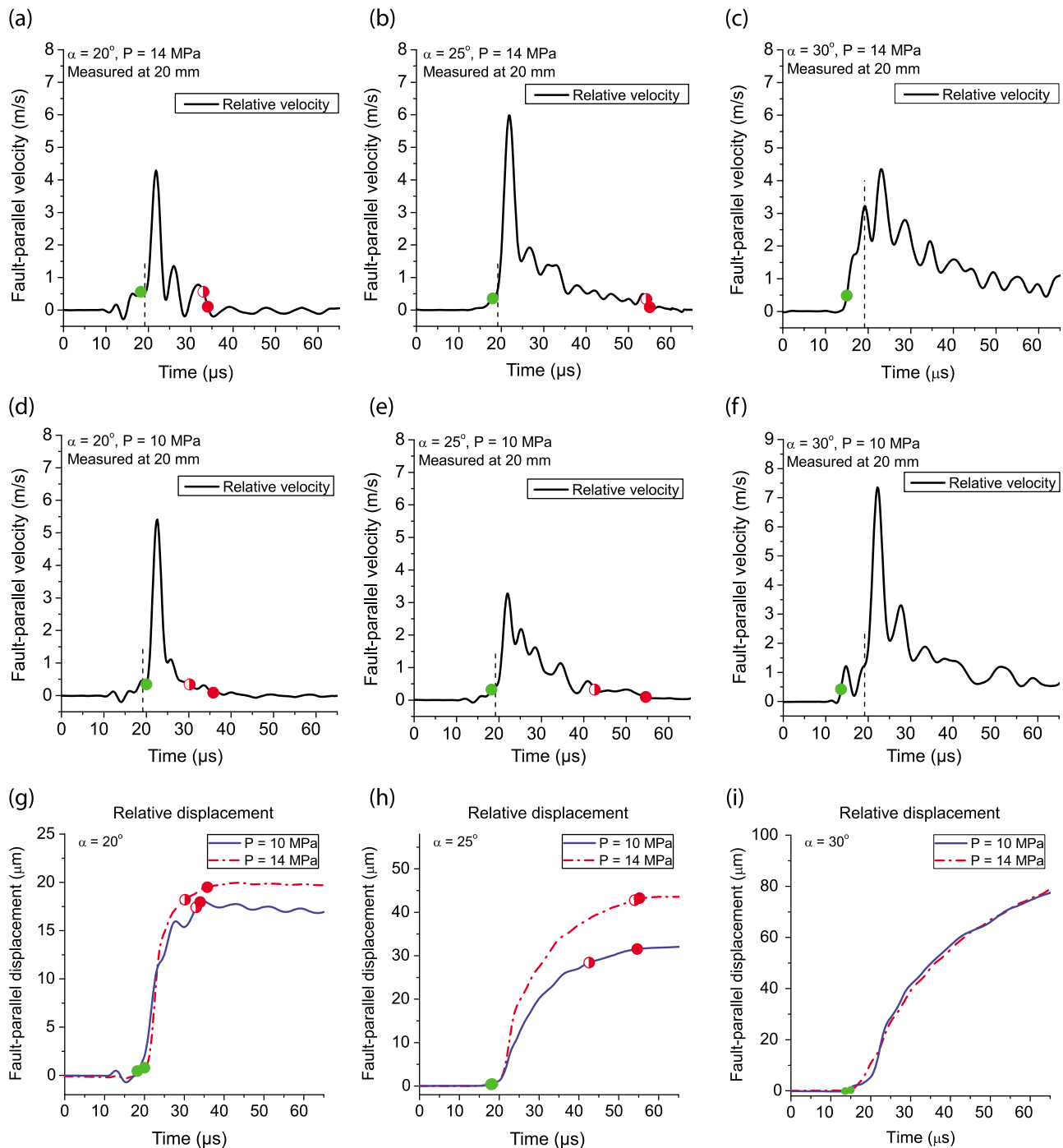


**Figure 7.** Variation of rupture mode with the inclination angle  $\alpha$  and hence with the nondimensional shear prestress, illustrated using (left column)  $\alpha = 20^\circ$ , (middle column)  $\alpha = 25^\circ$ , and (right column)  $\alpha = 30^\circ$  for two values of the compressive load, (top row)  $P = 14$  MPa and (middle row)  $P = 10$  MPa. (bottom row) The relative displacement profiles for the two compressive loads. As  $\alpha$  increases from  $20^\circ$  to  $25^\circ$ , and then to  $30^\circ$ , the risetime increases, so that the rupture mode varies from a narrower pulse-like to a wider pulse-like, and then to a crack-like mode. Green and red dots indicate rupture initiation and locking times as defined in section 3.2.

interface locking within the observation window. We call such ruptures pulse-like. The rupture duration, or the pulse width, increases with the inclination angle, being about  $15 \mu\text{s}$  in the cases with  $\alpha = 20^\circ$  (Figures 7a and 7d) and about  $35 \mu\text{s}$  (for the more conservative locking criterion) in the cases with

$\alpha = 25^\circ$  (Figures 7b and 7e). The inclination angle of  $\alpha = 30^\circ$  results in crack-like ruptures, in the sense that there is no interface locking within the time of observation (Figures 7c and 7f). The difference between rupture durations, or rise-times, for the three inclination angles can be further visual-

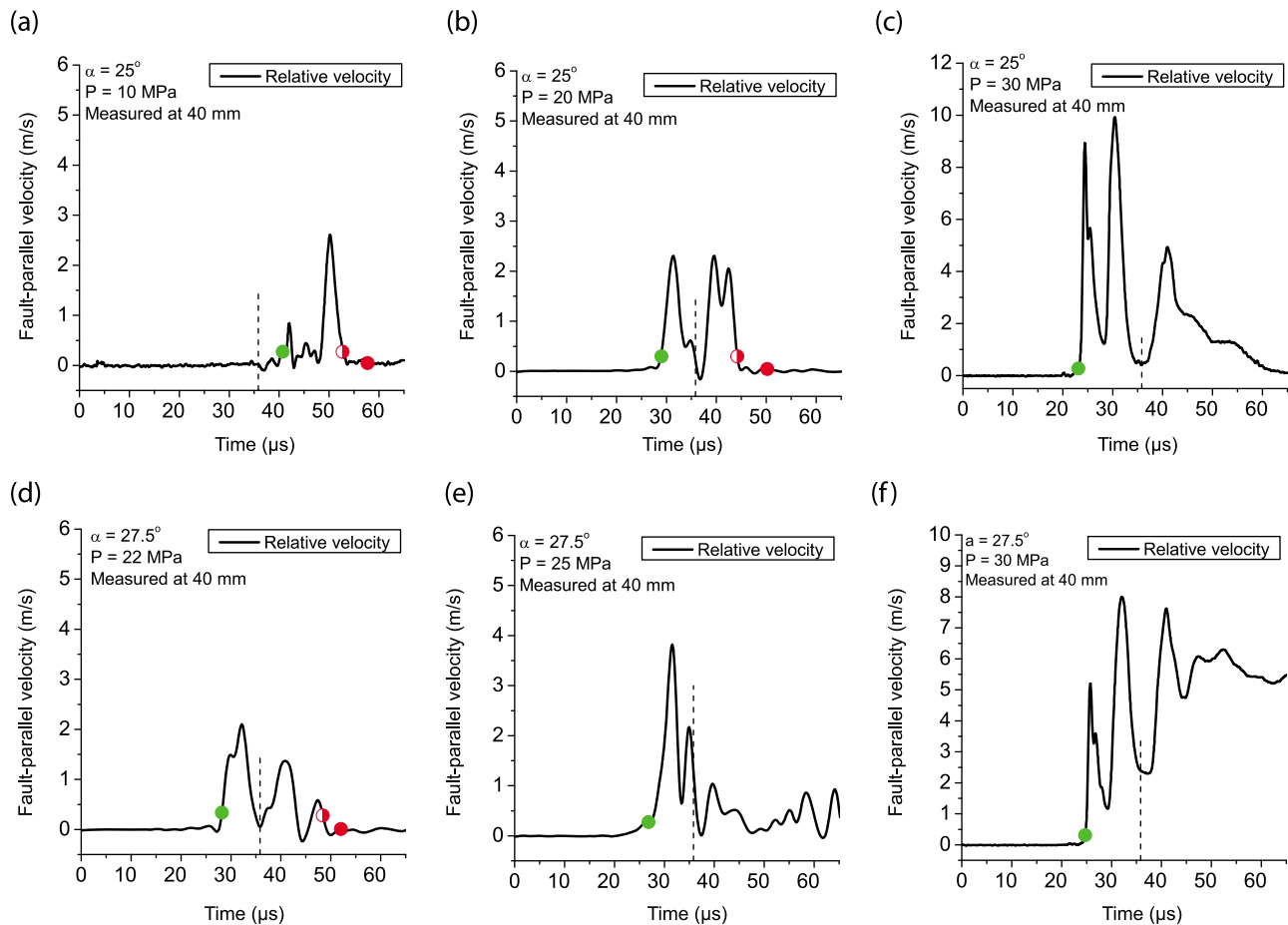


**Figure 8.** Variation of rupture mode with the compressive load  $P$  for (top)  $\alpha = 25^\circ$  and (bottom)  $\alpha = 27.5^\circ$ . Velocity histories are measured at the distance of 40 mm from the nucleation site. For both inclination angles, the risetime increases as  $P$  is increased. As before, the vertical dashed lines indicate the time of the first shear wave arrival.

ized through the plots of the relative fault-parallel displacement (Figures 7g–7i). The plots also show that crack-like modes lead to larger relative displacements; note that the vertical scale is different in Figures 7g–7i.

[37] Hence we find that rupture risetime increases with nondimensional shear prestress in our experiments. This is a direct experimental observation. Moreover, in the cases with the highest nondimensional shear prestress we consider, ruptures do not arrest locally during the experimental observation window. Hence we call these ruptures crack-like and refer to the observed increasing risetimes as a systematic variation from pulse-like to crack-like rupture modes. We caution, however, that we cannot exclude the possibility that what we call crack-like ruptures would actually become pulse-like if we could observe them for a longer time.

#### 4.2. Increase in Risetime With the Compressive Load

[38] The experimentally observed variation of the risetime and hence the rupture mode with nondimensional shear prestress described in section 4.1 is qualitatively consistent with theoretical predictions for ruptures on velocity-weakening interfaces (section 5). Another prediction of those theories is that the risetime would depend on the compressive load  $P$ , with larger values of  $P$  leading to more crack-like

ruptures (section 5). A hint of such dependence is already present in the results for  $P = 10$  MPa, as discussed by *Lu et al.* [2007], and  $P = 14$  MPa presented in section 4.1, as ruptures for the larger compression of 14 MPa have slightly longer durations. However, the differences are within experimental variability and cannot be conclusively attributed to larger values of  $P$ .

[39] In the present study, by considering a much wider range of compressive loads  $P$ , we indeed find that the rupture mode systematically varies from pulse-like to crack-like with increasing  $P$ . Note that the experiments with the larger values of  $P$  have been conducted specifically to verify the suggestion of *Lu et al.* [2007] that such dependence might exist, which they made based on their comparison of the initial set of experiments with the analysis of *Zheng and Rice* [1998]. Figure 8 illustrates the dependence of the risetime on  $P$  for two values of the inclination angle,  $\alpha = 25^\circ$  (top row,  $f_0 = 0.47$ ) and  $\alpha = 27.5^\circ$  (bottom row,  $f_0 = 0.52$ ). For both angles, the rupture varies from a narrower pulse, to a wider pulse, to what we call a crack-like mode, as the value of  $P$  is increased from 10 MPa to 30 MPa (top row) and from 22 MPa to 30 MPa (bottom row). The measurements presented in Figure 8 are done at the distance of 40 mm from the hypocenter. Figure 8 also shows that five

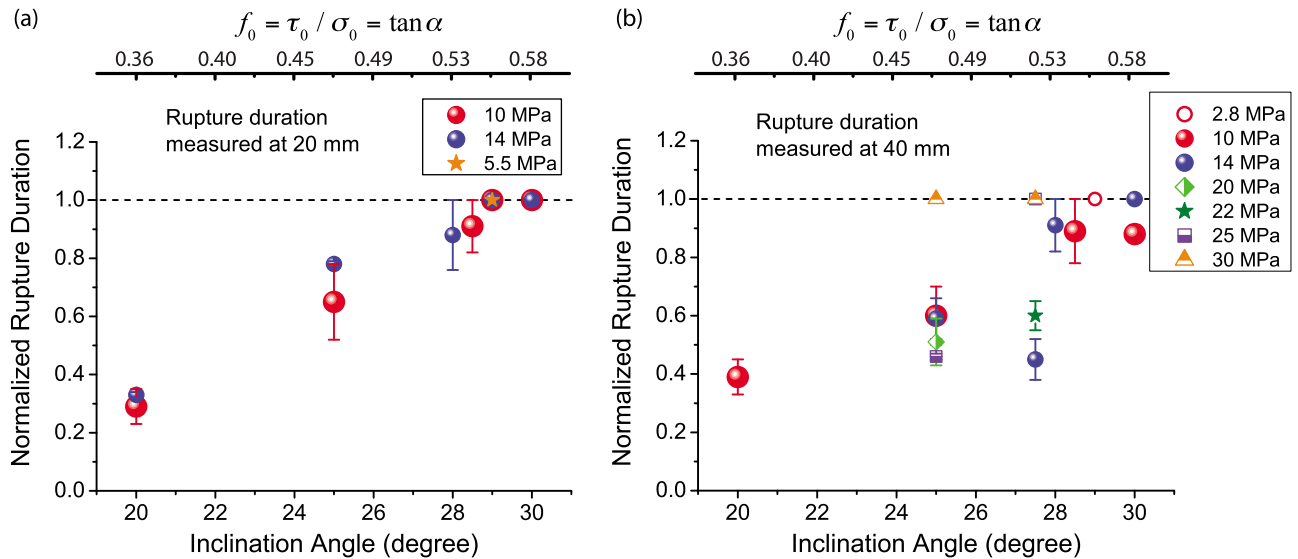


**Figure 9.** Collective analysis of local rupture duration for different inclination angles and compressive loads measured at the distance of (a) 20 mm and (b) 40 mm. The rupture duration is normalized by the total possible sliding time at the location, which is equal to the time window of observation minus the rupture arrival time. The normalized duration of 1 corresponds to crack-like ruptures and smaller values correspond to progressively narrower pulse-like ruptures.

out of the six presented cases have supershear speeds at this location, as evidenced by the rupture front arriving earlier than the shear wavefront marked by the vertical dashed line. The supershear transition and propagation are discussed in sections 7 and 8.

### 4.3. Collective Analysis of Local Rupture Duration

[40] The experimentally observed local rupture durations for a number of experiments with different inclinations angles  $\alpha$  and compressive loads  $P$  are summarized in Figure 9. In Figure 9, rupture duration for each experiment is normalized by the maximum potential sliding time, which is equal to the time window of observation minus the arrival time of the rupture front at the measurement location. This normalized rupture duration ranges from 0 (no sliding at the measurement location) to 1 (continuing sliding from the rupture arrival to the end of the observation). Crack-like ruptures correspond to the normalized rupture duration of 1, with smaller values indicating pulse-like ruptures of progressively shorter duration. For each experiment, the ends of the interval correspond to two estimates of the rupture duration, with a filled dot giving the average value. Figures 9a and 9b show rupture durations measured at 20 mm and 40 mm from the hypocenter, respectively. Angles below  $\alpha = 20^\circ$  were not studied, but those experiments would have likely produced dying pulses or no sliding at the measurement locations. For angles larger than  $\alpha = 30^\circ$ , prestress  $f_0$  would exceed the static friction coefficient of 0.6, which would cause the sliding to occur over the entire interface at once during the pre-loading stage.

[41] The collection of measurements in Figure 9 clearly shows that the inclination angle  $\alpha$ , and hence the nondimensional shear prestress  $f_0 = \tau_0/\sigma_0 = \tan\alpha$ , is the dominant factor in determining the risetime and hence rupture mode, with smaller angles and hence lower nondimensional shear

prestress favoring pulse-like ruptures of shorter duration. Note that for the inclination angle of  $\alpha = 28^\circ$ , the more conservative estimate of rupture duration gives the normalized rupture duration of 1, indicating that those ruptures may be fully crack-like. For angles  $\alpha = 29^\circ$  and  $\alpha = 30^\circ$ , the ruptures are clearly crack-like. Lower angles produce pulse-like ruptures for most values of  $P$ . For the wider range of compressive loads  $P$  explored at some angles (e.g.,  $\alpha = 25^\circ$  in Figure 9b), the dependence of rupture duration and hence rupture mode on  $P$  is also clearly visible.

### 5. Qualitative Agreement Between the Experimentally Observed Rupture Modes and Theoretical Predictions Based on Velocity-Weakening Friction

[42] The systematic variation of rupture modes from pulse-like to crack-like presented in section 4 is qualitatively consistent with the theoretical study of velocity-weakening interfaces by *Zheng and Rice* [1998]. The study showed that crack-like ruptures cannot exist under certain conditions and hence the only possibility for rupture propagation under those conditions is a self-healing pulse-like modes. Consider an interface with velocity-weakening friction  $\tau_{ss}(V)$ , prestressed with shear stress  $\tau_0$  and governed by the following 2-D elastodynamic equation expressed as an integral relationship between the shear stress  $\tau(x, t)$  and slip on the interface [*Perrin et al.*, 1995; *Zheng and Rice*, 1998]:

$$\tau(x, t) = \tau_0 + \phi(x, t) - \frac{\mu}{2c_s} V(x, t), \quad (2)$$

where  $\phi(x, t)$  is the functional of slip history on the interface and  $V(x, t)$  is the sliding velocity. For uniform sliding along the entire interface,  $\phi = 0$ . Following *Zheng and Rice* [1998], let us define  $\tau_{pulse}$  as the maximum value of prestress  $\tau_0$  that

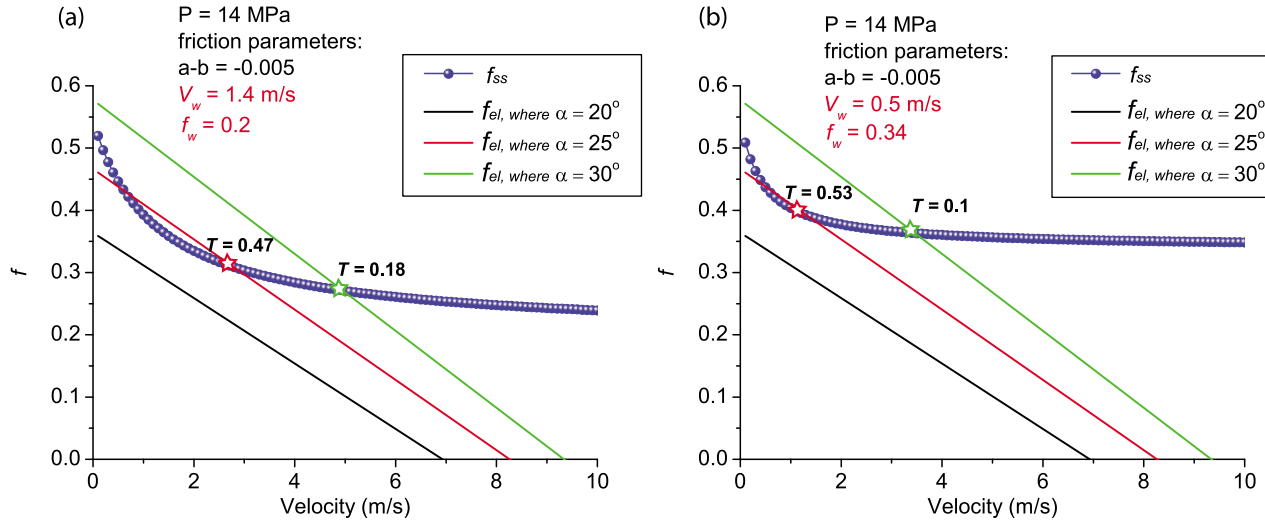


**Figure 10.** Illustration of the definition of the theoretical parameters  $\tau_{pulse}$  and  $T$  used to predict rupture mode in our analysis, based on the study of *Zheng and Rice* [1998], for two sets of velocity-weakening parameters: (a)  $f_w = 0.2$  and  $V_w = 1.4$  m/s and (b)  $f_w = 0.34$  and  $V_w = 0.5$  m/s. The dependence of the steady state friction coefficient on sliding velocity is shown as a dotted blue line. The (straight) lines of the normalized elastodynamic stress  $f_{el}(V) = \tau_{el}(V)/\sigma$  are also plotted for three different inclination angles.  $\alpha = 20^\circ$  corresponds to the shear prestress level lower than  $\tau_{pulse}$  and parameter  $T$  is not defined in that case. Higher angles of  $25^\circ$  and  $30^\circ$  result in the lines of elastodynamic stress intersecting the lines of steady state friction, with the corresponding values of parameter  $T$  given in Figure 10.

satisfies  $\tau_0 - \mu V/(2c_s) \leq \tau_{ss}(V)$  for all  $V \geq 0$ . *Zheng and Rice* [1998] proved that no crack-like solutions exists if  $\tau_0 < \tau_{pulse}$ , and hence such values of  $\tau_0$  have to correspond to either pulse-like solutions or no rupture. For larger values of  $\tau_0$ , their study defined a dimensionless parameter  $T$  that can be used to predict the rupture mode. Let us denote by  $V_{dyna}$  the larger of the two possible solutions of the equation  $\tau_0 - \mu V/(2c_s) = \tau_{ss}(V)$ . Then

$$T = \frac{d\tau_{ss}/dV}{d\tau_{el}/dV} \Big|_{V=V_{dyna}}, \quad (3)$$

where  $\tau_{el} = \tau_0 - \mu V/(2c_s)$ . That is, parameter  $T$  is the ratio of the slopes of the steady state friction curve  $\tau_{ss}$  and the elastodynamic stress  $\tau_{el}$  evaluated at their intersection  $V = V_{dyna}$ . If  $T$  does not exist (which occurs for  $\tau_0 < \tau_{pulse}$ ), the rupture mode is either pulse-like or there is no rupture propagation. When  $T$  exists, it is a nondimensional scalar between zero and one.  $T = 1$  corresponds to  $\tau_0 = \tau_{pulse}$  and hence values of  $T$  close to 1 correspond to pulse-like modes. As  $T$  decreases to 0, the ruptures become crack-like.

[43] To apply the analysis of *Zheng and Rice* [1998] to our experiments, let us assume that the interface is governed by the Dieterich-Ruina rate-and-state friction law [Dieterich, 1979; Dieterich, 1981; Ruina, 1983; Dieterich and Kilgore, 1994; Dieterich and Kilgore, 1996; Lapusta et al., 2000] enhanced with additional velocity weakening at high slip velocities, as appropriate for flash heating. For steady state sliding, the friction law reduces to

$$\tau_{ss}(V) = \sigma \left( f_w + \frac{f_* + (a-b) \ln(V/V_*) - f_w}{1 + V/V_w} \right), \quad (4)$$

where  $f_*$  and  $V_*$  are the reference friction coefficient and slip velocity, respectively,  $a$  and  $b$  are rate-and-state friction coefficients,  $V_w$  is the characteristic slip velocity for flash heating, and  $f_w$  is the residual friction coefficient at high sliding rates. Based on preliminary low-velocity friction measurements for Homalite interfaces (collaboration with B. Kilgore, N. Beeler, and C. Marone), we use the following values:  $f_* = 0.6$ ,  $V_* = 1 \times 10^{-6}$  m/s, and  $b - a = 0.005$ . Since there are no high-velocity friction measurements for Homalite, the values of  $f_w$  and  $V_w$  have to be selected based on indirect inferences from previous studies and the flash-heating theory [Rice, 2006]. *Lu et al.* [2009] showed, through numerical simulations of dynamic ruptures on slip-weakening interfaces, that supershear transition distances experimentally determined by *Xia et al.* [2004] can be matched by models with a range of dynamic friction coefficients, if suitable modifications in other parameters are assumed. *Lu et al.* [2009] used dynamic friction coefficients 0.2 and 0.34 as examples. Based on the values of other parameters needed to fit the transition distances, *Lu et al.* [2009] argued that 0.2 and 0.34 may represent the lower and upper bounds of the actual dynamic friction coefficient. The residual friction coefficient  $f_w$  in the velocity-dependent friction description used in this study is analogous to the dynamic friction coefficient of linear slip-weakening friction used by *Lu et al.* [2009], and so we consider values of  $f_w = 0.2$  and  $f_w = 0.34$  here. The application of the flash-heating theory of *Rice* [2006] to Homalite results in the range of 0.2 m/s to 2 m/s for the characteristic flash-heating velocity  $V_w$ , assuming plausible ranges for inputs. We use the following two sets of parameters to illustrate the predictions of *Zheng-Rice* theory:  $f_w = 0.2$ ,  $V_w = 1.4$  m/s (Figure 10a and Figure 11) and  $f_w =$

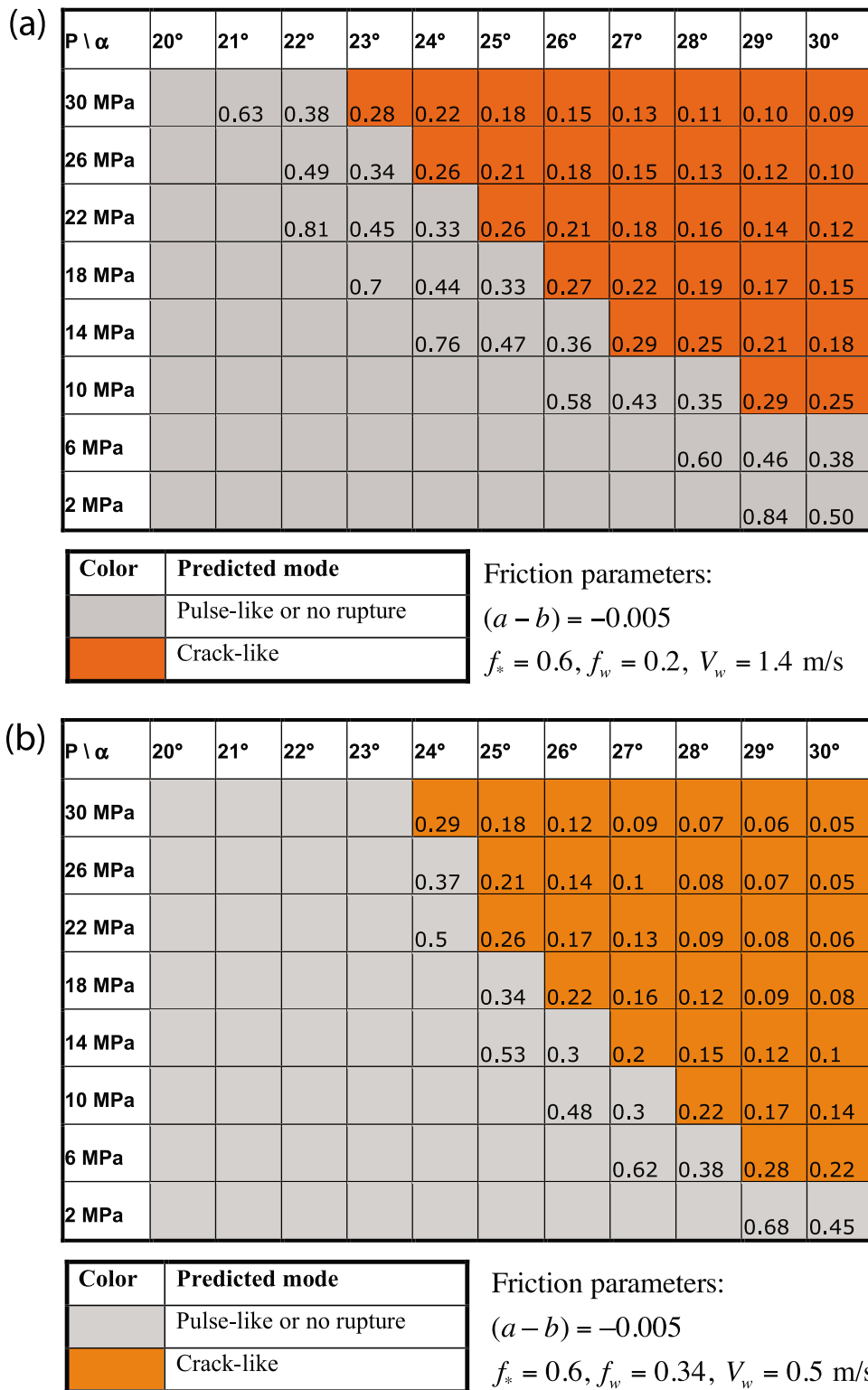


**Figure 11.** Values of the mode-predicting parameter  $T$  for the ranges of inclination angles and compressive loads explored in our experiments, computed assuming the friction law (equation (4)) and using (a)  $f_w = 0.2$  and  $V_w = 1.4$  m/s and (b)  $f_w = 0.34$  and  $V_w = 0.5$  m/s. Other friction parameters are specified in the text. Values of  $T$  close to 0 predict crack-like modes, while values close to 1 predict pulse-like modes. Empty cells correspond to experimental conditions for which parameter  $T$  is not defined, predicting either a pulse-like rupture or no rupture. The region  $T < 0.3$  is shown in orange, to qualitatively indicate the experimental parameter space that is predicted to correspond to crack-like ruptures. The separating value of 0.3 is chosen based on simulations of *Zheng and Rice* [1998].

0.34,  $V_w = 0.5$  m/s (Figure 10b and Figure 11). We continue to assume that normal stress  $\sigma$  is approximately equal to the initial normal stress  $\sigma_0$  at the location where we interpret the rupture mode. The basis for this assumption is discussed in section 6.1.

[44] Figure 10 illustrates the elastodynamic stress  $\tau_{el} = \tau_0 - \mu V/(2c_s)$  and the steady state friction dependence  $\tau_{ss}(V)$ , the comparison of which is used to define the mode-predicting parameters  $\tau_{pulse}$  and  $T$  as described above. The normalized steady state friction

$$f_{ss}(V) = \tau_{ss}(V)/\sigma = f_w + \frac{f_* + (a - b) \ln(V/V_*) - f_w}{1 + V/V_w} \quad (5)$$

and the normalized elastodynamic stress

$$f_{el}(V) = \tau_{el}(V)/\sigma = \tan \alpha - \frac{\mu}{2c_s} \frac{V}{P \cos^2 \alpha} \quad (6)$$

are plotted. From the last expression, we see that both experimental parameters,  $\alpha$  and  $P$ , affect  $f_{el}(V)$  and hence the values of  $\tau_{pulse}$  and  $T$ . In both panels of Figure 10,  $P = 14$  MPa and three representative cases with the inclination angles of  $20^\circ$ ,  $25^\circ$ , and  $30^\circ$  are considered.  $f_w = 0.2$ ,  $V_w = 1.4$  m/s and  $f_* = 0.34$ ,  $V_w = 0.5$  m/s are adopted in Figures 10a and 9b, respectively. Both panels illustrate the same qualitative features. For  $\alpha = 20^\circ$ , the elastodynamic stress (black line) is below the steady state friction (blue dotted line) for all  $V \geq 0$  and no intersection exists between the two curves. According to the analysis of *Zheng and Rice* [1998], in this case the rupture would either proceed in a pulse-like mode or not at all, i.e., the rupture would arrest. This is consistent with our experimental results that indicate pulse-like ruptures for all cases with  $\alpha = 20^\circ$  that have been studied (Figure 7). As the inclination angle increases, the nondimensional prestress grows, and the elastodynamic stress lines move up; their intersection with the friction curve defines the nondimensional parameter  $T$  which varies from  $T = 1$  when the two lines touch to values approaching zero for intersections at higher values of  $V$ . The trend indicates that local slip duration should increase for larger inclination angles, as observed in our experiments.

[45] To compare the predictions of *Zheng and Rice* [1998] with the results of our experiments for all experimental parameters, we compute the values of parameter  $T$  for  $P$  from 2 MPa to 30 MPa and for  $\alpha$  from  $20^\circ$  to  $30^\circ$  (Figure 11). For a fixed value of  $P$ , e.g.,  $P = 14$  MPa, parameter  $T$  decreases from values close to 1 to values close to zero as the inclination angle  $\alpha$  increases, predicting variation from pulse-like to crack-like rupture modes and hence increase in risetimes; empty cells of Figure 11 correspond to parameter regimes in which parameter  $T$  does not exist, which predicts that the rupture is either a pulse or there is no rupture. This is consistent with experimentally observed variation of rupture mode with the inclination angle  $\alpha$  (section 4.1). For a fixed value of  $\alpha$ , e.g.,  $\alpha = 25^\circ$ , parameter  $T$  again decreases from values close to 1 to values close to zero as the compressive load  $P$  increases, predicting variation from pulse-like to crack-like modes. This is consistent with the experimentally observed variation of rupture mode with the compressive load  $P$ . Overall, higher values of either  $\alpha$  or  $P$  favor crack-

like rupture in experiments as well as in the theoretical prediction; the corresponding cells of Figure 11 are marked with orange, using  $T = 0.3$  as the cutoff value based on the numerical study of *Zheng and Rice* [1998]. Hence we find that the systematic variation of rupture modes observed in the experiments, both with nondimensional shear prestress and with the absolute levels of stresses as parameterized by the compressive load, is consistent with the theoretical predictions of *Zheng and Rice* [1998] based on velocity-weakening friction.

## 6. Effect of Nucleation Procedure

[46] The comparison between experimental results and velocity-weakening theories in section 5 assumes that fault-normal stress is not altered outside the nucleation region. The rupture initiation procedure reduces normal stress locally in the nucleation region, and that effect might propagate along the interface, creating lower friction resistance and potentially providing an alternative explanation for the variation in rupture modes. In this section, we study this and other potential effects of the nucleation procedure.

### 6.1. Measurements of Fault-Normal Motion

[47] To assess whether there are notable changes in fault-normal stress  $\sigma$  outside the nucleation region, we have conducted several experiments in which the fault-normal particle velocity histories above and below the interface were measured at the same location (20 mm) and with a similar setup as for the fault-parallel velocity measurements. The configuration of the measurements is illustrated in Figure 12. Two reflective membranes are positioned 20 mm away from the hypocenter. Laser velocimeters are focused on two membrane edges separated by the distance of 0.5 mm. The difference between the two fault-normal measurements would indicate changes in the fault-normal stress. Negative values of relative velocity would indicate that the two measurement locations are moving closer together and hence correspond to increase in fault-normal compressive stress  $\sigma$ ; positive values would correspond to decrease of the fault-normal compression. Because the experiments are designed to induce in-plane shear rupture, fault-normal measurements are expected to be much smaller than the fault-parallel ones. This reality requires much higher accuracy of the alignment of the laser beams. Other factors may affect the measurement, such as potential slight nonplanarity of membrane surfaces and its effect due to relative sliding motion of the two measurement locations.

[48] We present fault-normal measurements for two experiments conducted with the inclination angles of  $20^\circ$  and  $30^\circ$  (Figure 13), which are the lowest and highest inclination angles used in experiments. The individual velocity measurements above and below the interface generally coincide (Figures 13a and 13b), showing that the two points move together for the entire duration of the experiment. This suggests that there are no significant changes in the fault-normal stress. To quantify the small differences between fault-normal velocities above and below the interface, we compute the relative fault-normal velocity (Figures 13c and 13d) as well as the relative fault-normal displacement (Figures 13e and 13f). The relative normal

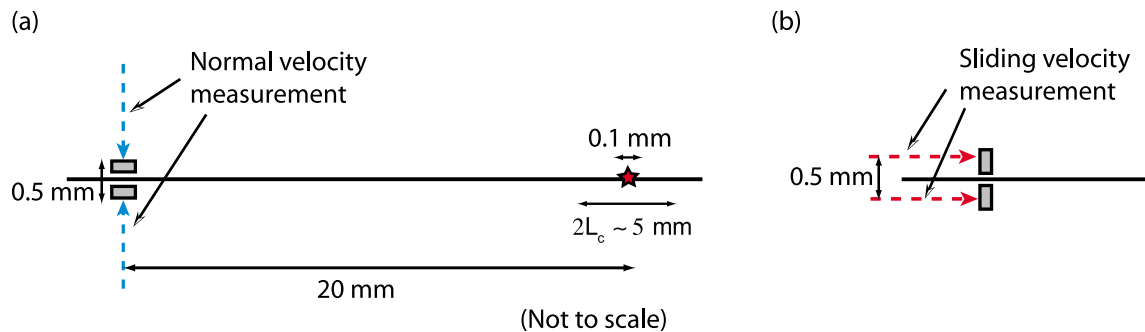


**Figure 12.** Schematic illustration of the experimental setup for fault-normal velocity measurements. Two measurement locations are separated by 500  $\mu\text{m}$ . Note that the exploding wire is 100  $\mu\text{m}$  in diameter and the distance between the wire and the measurements location is 20 mm. Any wave radiated from the nucleation site will continuously decay as it propagates.

measurements are about two orders of magnitude smaller than the fault-parallel measurements (Figures 7 and 8), as expected. To emphasize this discrepancy, the ranges of the  $y$  axes in Figure 13 are comparable to the ranges of the fault-parallel measurements. The insets in Figures 13c–13f show the relative normal velocities and displacements in more detail, for the time period that starts with the approximate  $P$  wave arrival time of 10  $\mu\text{s}$  and includes the period of the most active sliding between 20  $\mu\text{s}$  and 30  $\mu\text{s}$ . We see that, for both angles, the two measurement points get closer between 10  $\mu\text{s}$  and 30  $\mu\text{s}$ , by about 0.1  $\mu\text{m}$  for  $\alpha = 20^\circ$  and 0.3  $\mu\text{m}$  for  $\alpha = 30^\circ$ . Note that the two measurement locations have the distance of 500 microns between them.

[49] Hence the fault-normal measurements reveal no reduction of normal stress during sliding; on the contrary, they point to larger compression. This means that the observed ruptures are not driven by normal stress reduction propagating along the interface from the nucleation region. In the case of  $\alpha = 20^\circ$ , the sliding stops at about 30 to 35  $\mu\text{s}$  (Figure 7a); the relative normal velocity and displacement histories show nothing special occurring during those times; in fact, the variations in fault-normal quantities are minimal in that time interval. Hence the arrest of sliding for  $\alpha = 20^\circ$  is likely caused by variations of the friction coefficient due to velocity-weakening friction, as advocated in section 5, and not by normal stress changes.

[50] We caution that the inferred fault-normal relative displacements of 0.1 to 0.3  $\mu\text{m}$  are quite small and may be testing the limits of our resolution. While relative fault-normal velocity measurements are largest during the time interval of most active slip, from 20  $\mu\text{s}$  to 30  $\mu\text{s}$ , they do not exhibit a coherent change for that time period but rather have an oscillatory nature. One would expect the largest measurement errors to occur when the membranes, which serve as focusing locations for the laser beams, are moving, mostly in the direction perpendicular to the beams. The motion may affect the accuracy of the velocimeters, and it may lead to the measurement reflecting the roughness of the membrane surfaces rather than any fault-normal motion. However, the consistent increase of compression that we observe in the presented measurements and in several other experiments suggests that decrease in the fault-normal compression during sliding is unlikely.

## 6.2. Influence of Nucleation Strength

[51] While in section 6.1 we argue that normal stress reduction due to the explosion is not observed at the measurement locations, the nucleation procedure can still affect rupture propagation through other means [Festa and Vilotte, 2006; Shi and Ben-Zion, 2006; Liu and Lapusta, 2008; Shi et al., 2008; Lu et al., 2009]. For example, different explosions could create different history of sliding in the initiation region, releasing a different shear wavefield and starting a domino effect that may significantly alter the rupture development.

[52] As a first step toward understanding those dependencies, here we study the effect of the explosion intensity. The results of two experiments with different charging voltage for the explosion are shown in Figure 14. We see that the rupture duration in the two cases is similar, and the resulting rupture is pulse-like. At the same time, the peak relative velocity is higher for the higher voltage. A possible explanation is that the stronger explosion creates larger sliding velocities and hence larger fault-parallel relative displacements in the nucleation region, and the radiated waves carry this information, affecting the peak sliding velocities further along the interface. Based on these and similar experiments, we conclude that, as long as the nucleation procedure is strong enough to trigger the rupture, the mode of the rupture would be independent of the explosion strength.

## 7. Rupture Speeds of Pulse-Like and Crack-Like Modes

### 7.1. Observations of Supershear Pulses and Cracks

[53] The experimental measurements of relative fault-parallel velocity presented in section 4 provide a number of examples of both supershear crack-like ruptures (Figures 7c, 7f, 8c, 8e, and 8f) and supershear pulse-like ruptures (Figures 7a, 8b, and 8d). The speeds are clearly supershear in those cases as rupture arrival times (indicated by green dots) at the measurement locations are smaller than arrival times of the shear wave (indicated by vertical dashed lines). Ruptures typically transition to supershear speeds after a period of sub-Rayleigh propagation, and the distance between the location of the crack initiation and the location of supershear transition is called the transition distance

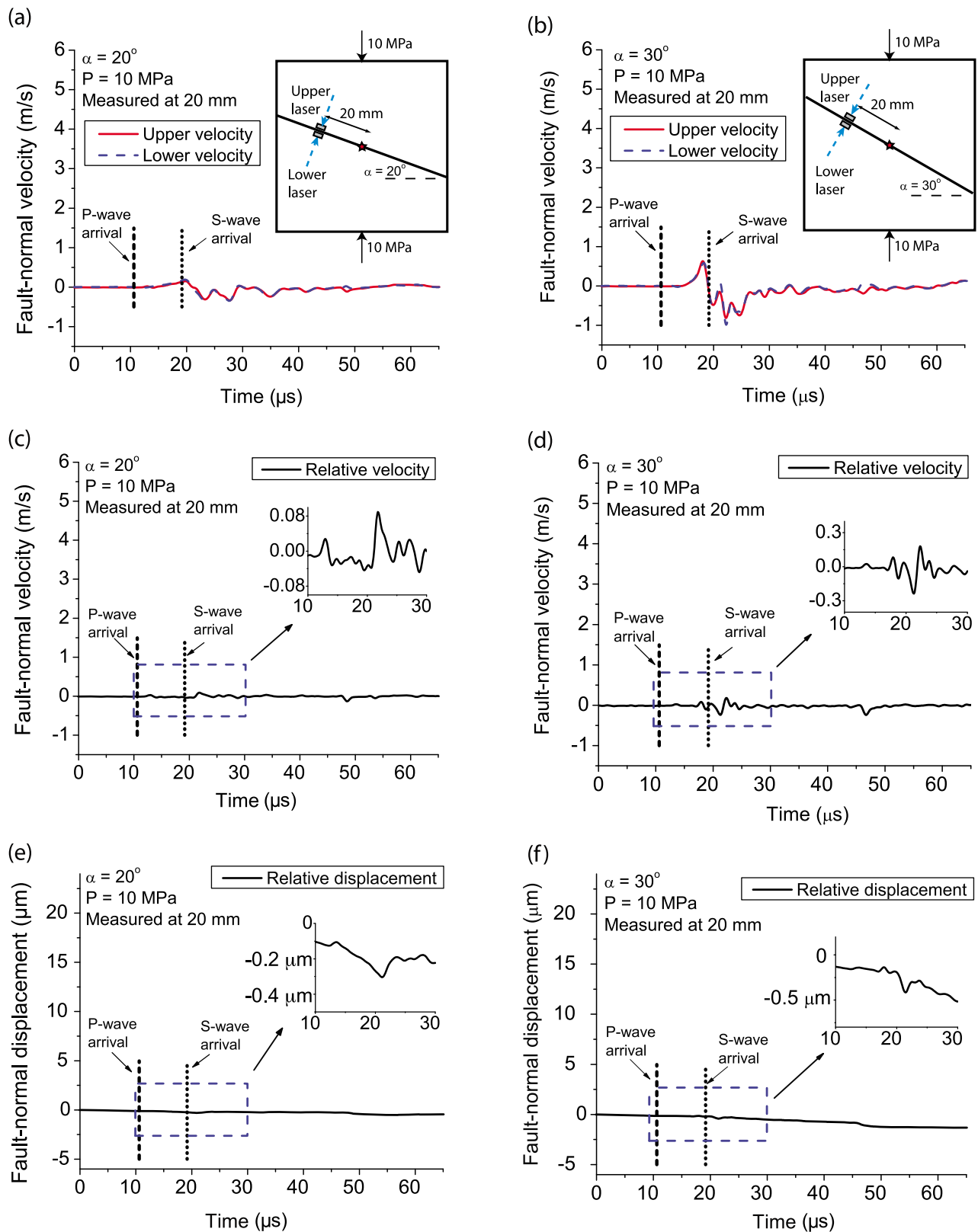


**Figure 13.** Fault-normal measurements at the distance of 20 mm for the experiments with (left)  $\alpha = 20^\circ$  and (right)  $\alpha = 30^\circ$ . The compressive load is  $P = 10$  MPa for both cases. (a and b) Fault parallel velocity measurements above and below the interface. (c and d) The relative fault-normal velocity profile. The inset gives the detailed view for the time window between 10 and 30  $\mu$ s, during which the  $P$  wave arrives and largest fault-parallel velocities are recorded. (e and f) The relative fault-normal displacement between two measurement points. Negative values correspond to more compression.

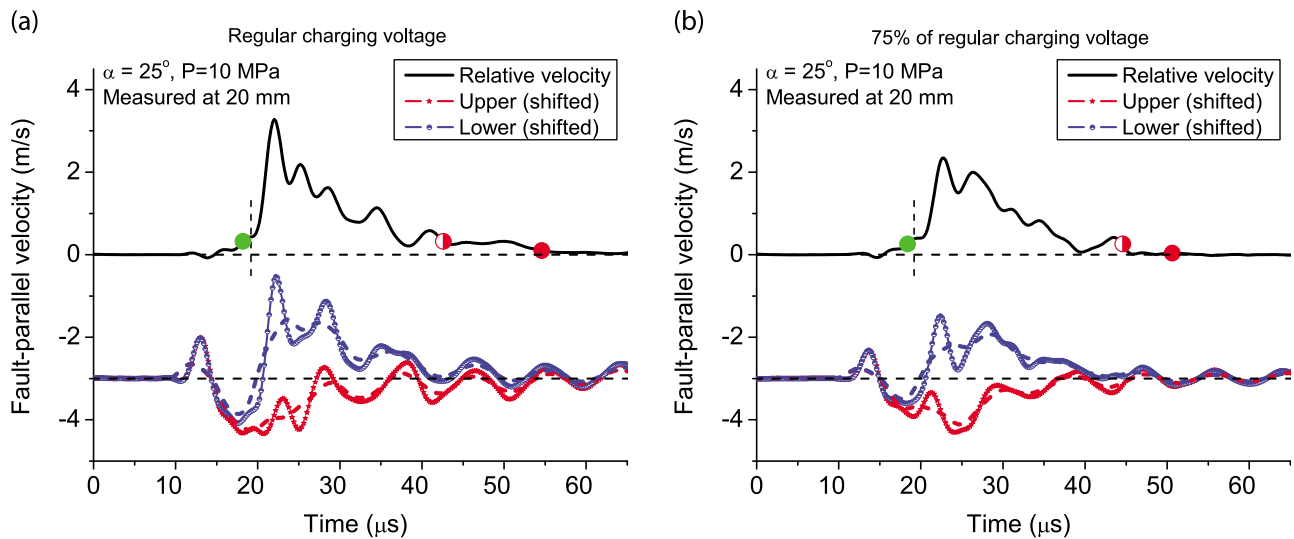


**Figure 14.** Comparison of fault-parallel velocity histories obtained with different explosion intensity for  $\alpha = 25^\circ$  and  $P = 10$  MPa. (a) The capacitor bank used for the wire explosion is charged with the regular voltage of 1600 V. (b) The charging voltage is reduced to 75% of the regular value. The peak slip velocity in Figure 14b is reduced but the rupture duration is similar.

[Andrews, 1976; Xia *et al.*, 2004; Rosakis *et al.*, 2007]. The ruptures that are supershear in Figures 7 and 8 have transition distances smaller than 20 mm and 40 mm, respectively, as Figures 7 and 8 show velocity measurements at those locations. Note that transition distances in our experiments tend to be larger than the ones reported by Xia *et al.* [2004]. The difference can be attributed to a different surface preparation and hence different friction properties.

[54] Representative cases of supershear pulse-like and crack-like ruptures are presented in Figure 15 for  $P = 14$  MPa and three inclination angles  $\alpha$  of 27.5, 28, and 30 degrees. For  $\alpha = 27.5^\circ$ , the rupture is clearly pulse-like, with the sliding stopping within the observation window (Figure 15a). The slip history shown in Figure 15a consists of two pulses, a supershear pulse followed by a subshear pulse. Such a sliding history could be indicative of the mother-daughter transition mechanism [Burrige, 1973; Andrews, 1976], in which a supershear “daughter” rupture nucleates in front of the main sub-Rayleigh “mother” rupture. In numerical simulations of that mechanism [e.g., Lu *et al.*, 2009], the daughter and mother rupture become connected later and propagate as a single rupture. The profile in Figure 15a could be interpreted as evidence for the mother-daughter transition mechanism. However, ruptures can transition to supershear speeds by direct change of speeds at the rupture tip [Liu and Lapusta, 2008; Lu *et al.*, 2009]. Numerical simulations show [Liu and Lapusta, 2008; Lu *et al.*, 2009] that, in the case of the direct transition with no daughter crack, the supershear portion of the rupture may still look partially or fully disconnected from the rest of the rupture, similarly to the profile in Figure 15a. This is due to the stress changes, and hence sliding velocity changes, caused by the combination of shear waves and Rayleigh waves that are left behind the supershear rupture tip. Hence further study is needed to conclusively determine the transition mechanism in our experiments, as discussed by Lu *et al.* [2009].

[55] Figure 15b shows the superposition of the photoelastic fringe pattern at the time of  $t = 44 \mu\text{s}$  and the slip velocity measurements from Figure 15a reinterpreted with respect to the interface locations as explained in section 3.1. The image contains a clear circular shear wavefront and a ring-like fringe structure with a stress concentration tip on the interface ahead of the shear wave. That stress concentration corresponds to the supershear rupture tip, as indicated by the superposition with the velocity measurements. An interesting observation is the absence of Mach lines emitted from the supershear rupture tip; such Mach lines are a common feature of supershear ruptures [Rosakis, 2002; Xia *et al.*, 2004; Rosakis *et al.*, 2007]. The Mach lines are not formed at the special supershear rupture speed equal to  $\sqrt{2} c_s$  [Rosakis, 2002]. Hence the evidence for supershear propagation from the slip velocity history in Figure 15a and the absence of Mach lines in the photoelastic image can be reconciled if the rupture speed is  $\sqrt{2} c_s$ . In section 7.2, we show that the rupture speed in this case is indeed close to  $\sqrt{2} c_s$ .

[56] According to the results in sections 4 and 5, one can obtain crack-like ruptures by increasing the inclination angle. At the same time, the ruptures would remain supershear, as larger inclination angles translate into larger nondimensional prestress which favors supershear transition [Andrews, 1976, section 8]. This is demonstrated in Figures 15c and 15d. When the inclination angle is increased to 28 degrees, the rupture remains supershear but the sliding zone widens, producing either a wider pulse according to the locking criterion based on slip velocity or even a crack-like rupture according to the more conservative criterion based on residual slip (Figure 15c). The supershear rupture tip is well ahead of the shear wave, indicating that the transition distance is shorter in this case than in the case of Figure 15a, and/or that the rupture speed may be higher. Figure 15d shows the case of  $\alpha = 30^\circ$ , an angle which results in a supershear crack-like rupture as judged by measurements at the location of 20 mm

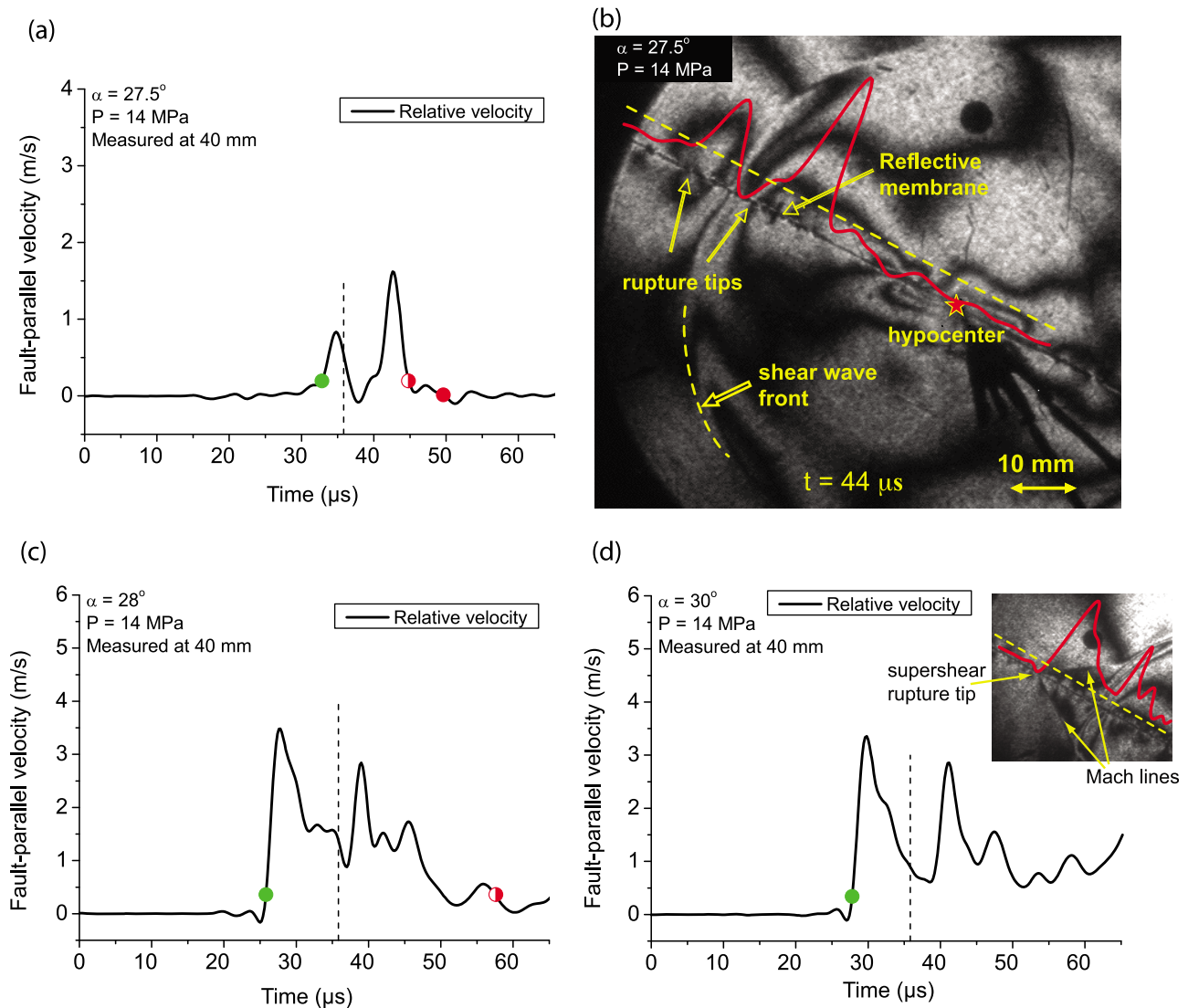


**Figure 15.** Representative cases of supershear pulse-like and crack-like ruptures. Fault-parallel relative velocity histories shown are measured at 40 mm in experiments with  $P = 14$  MPa. (a)  $\alpha = 27.5^\circ$  results in a supershear pulse-like rupture. (b) Superposition of the photoelastic image captured at  $44 \mu\text{s}$ , and the velocity measurement from Figure 15a. The rupture front is clearly ahead of the circular shear wavefront, a part of which is marked with a curved yellow line. (c)  $\alpha = 28^\circ$  results in a nearly crack-like rupture that has almost arrested at the end of the observation window. (d)  $\alpha = 30^\circ$  produces a supershear rupture that is clearly crack-like. The inset shows a part of the corresponding photoelastic image with the resulting Mach lines.

from the hypocenter (Figure 7c). At 40 mm, the rupture is still crack-like, in the sense that sliding does not arrest in the time window of observation, and the rupture speed is clearly supershear. The insert gives a photoelastic image with two clear Mach lines.

## 7.2. Evolution of Rupture Speeds for Supershear Pulses and Cracks

[57] To further analyze the supershear transition and propagation of different rupture modes, we infer the rupture speed evolution of the pulse-like and crack-like ruptures discussed in section 7.1. The rupture speed history is determined using the sequence of photoelastic images obtained by the high-speed camera. The tip of the rupture is identified in

each image and the rupture speed is computed as the ratio of the rupture tip advance and interimage time. The rupture speed is then averaged for three neighboring images. The location of the jump from sub-Rayleigh to supershear speeds is confirmed by the appearance of two concentrations of fringes in photoelastic images, one for the supershear crack tip and the other for the remnant of the subshear crack tip. For the images that have well-developed Mach lines, the inferred supershear values of the rupture speed  $v_r$  are corroborated by measuring the angle  $\beta$  that the Mach lines make with the interface and computing the rupture speed by the equation  $v_r = c_s / \sin \beta$ .

[58] We find that the pulse-like rupture has a larger transition distance and smaller supershear speeds than the

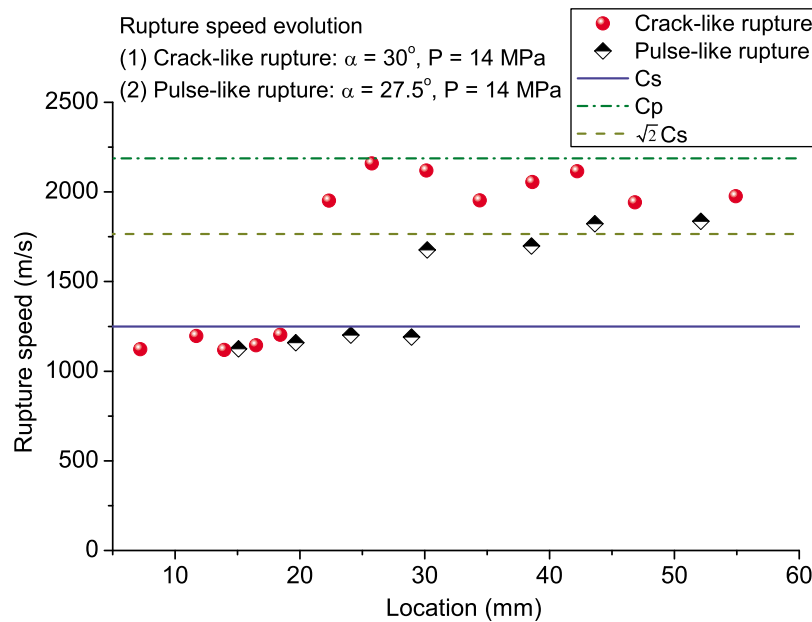


**Figure 16.** Evolution of the rupture speed for a pulse-like rupture (diamonds) and a crack-like rupture (circular dots). Both ruptures have supershear speeds within the open interval between  $\sqrt{2} c_s$  and  $c_p$ . The pulse-like rupture has lower supershear speeds than the crack-like rupture. Both observations are consistent with theories based on velocity-weakening interfaces.

crack-like rupture (Figure 16). Both ruptures have subshear speeds initially, and then rupture speeds abruptly change to supershear speeds. The pulse-like rupture, obtained under the experimental conditions  $P = 14$  MPa and  $\alpha = 27.5^\circ$ , has the transition distance of about 30 mm and supershear speeds close to  $\sqrt{2} c_s$ . The crack-like rupture, obtained under the experimental conditions  $P = 14$  MPa and  $\alpha = 30^\circ$ , has the transition distance of about 20 mm and supershear speeds within the interval between  $\sqrt{2} c_s$  and  $c_p$ . The inferred transition distances and rupture speeds are consistent with the rupture arrival times at the location of 40 mm (Figures 15a and 15d). The pulse-like rupture arrives later at this location than the crack-like rupture, which is consistent with lower rupture speeds for the pulse-like rupture.

[59] The inferred supershear rupture speeds are in qualitative agreement with the theoretical analysis of supershear rupture propagation on interfaces governed by velocity-weakening friction by *Samudrala et al.* [2002]. Their asymptotic analysis determined that the interval of rupture speeds between  $\sqrt{2} c_s$  and  $c_p$  corresponds to stable rupture growth and that higher interface prestress corresponds to higher rupture speeds. This is exactly what we observe in our experiments. First, both pulse-like and crack-like ruptures develop supershear speeds in the interval between  $\sqrt{2} c_s$  and  $c_p$ . Second, the pulse-like rupture, which corresponds to a lower inclination angle and hence lower nondimensional shear prestress, has lower supershear rupture speeds.

## 8. Map of Rupture Modes and Speeds Under a Range of Experimental Conditions

[60] To summarize our findings in terms of both rupture modes and rupture speeds, we create a diagram (Figure 17)

that indicates, for each set of experimental conditions, whether the rupture is crack-like or pulse-like, and whether its eventual propagation speed is sub-Rayleigh or supershear. For the determination of rupture mode, we use fault-parallel velocity measurements at the location of 40 mm if they are available; otherwise, we use the measurements at 20 mm. The rupture is marked as supershear if it transitions to supershear speeds within the observation domain, which extends 60 mm from the nucleation location (or 120 mm if the interface on both sides of the hypocenter is considered). Otherwise, the ruptures are marked sub-Rayleigh. This classification results in four rupture categories: supershear crack, sub-Rayleigh crack, supershear pulse, and sub-Rayleigh pulse. They are labeled by different symbols in Figure 17.

[61] The diagram clearly indicates variation from pulse-like to crack-like rupture modes as the inclination angle (and hence the nondimensional shear prestress) and the compressive load are increased. The domains of pulse-like and crack-like behavior are separated by an orange dashed line. The diagram can be directly compared to Figure 11 of theoretical predictions based on *Zheng and Rice* [1998] and our analysis in section 4. The map of the experimental results and the table of the theoretical predictions are in qualitative agreement, with the upper right corner of both corresponding to crack-like ruptures and the rest of experimental conditions corresponding to pulse-like ruptures or no rupture. The qualitative agreement between the experiments and theoretical predictions points to the importance of velocity-weakening friction, as discussed in section 5. Note that the boundary between the two regions has a different shape in the map of experimental results and in the theoretically constructed table. This could be partially due to the general nature of the theoretical analysis, which ignores the

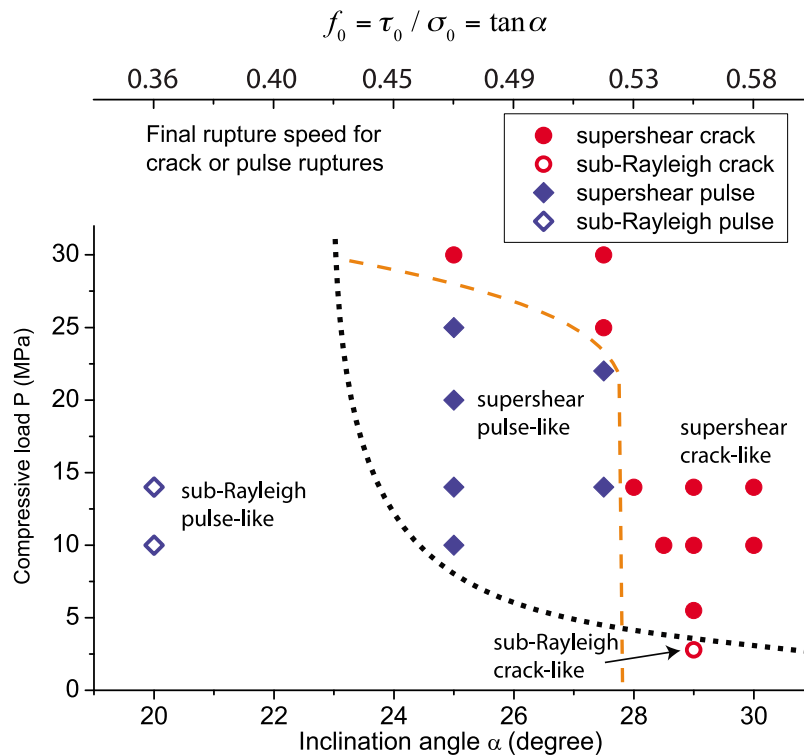


**Figure 17.** Map of pulse-like (diamonds) versus crack-like (circular dots) modes and sub-Rayleigh (open symbols) versus supershear (filled symbols) rupture propagation observed in our experiments. The boundary between pulse-like and crack-like modes (orange dashed line) is drawn based on the experimental results to qualitatively separate the two regimes. The boundary between ruptures that do and do not have supershear propagation (black dotted line) is drawn based on the theoretical analysis as discussed in the text.

influence of the initiation procedure and assumes a friction law that is plausible but not yet verified for Homalite, and partially due to potential viscoelastic effects in Homalite, which would create additional damping of energy and may turn what would be a crack-like mode in a purely elastic material into a pulse-like one. Some of the cases studied exhibit hints of such viscoelastic behavior. For example, in the case of  $\alpha = 28^\circ$  and  $P = 14$  MPa, the rupture is clearly crack-like at the location of 20 mm. However, the measurements at 40 mm (Figure 15c) have lower sliding velocity behind the rupture tip. Indeed, the locking criterion based on sliding velocity (section 3.2) indicates that interface healing occurs before the end of the observation time window. We mark this case as crack-like in Figure 17, as the more conservative locking criterion, the one based on residual slip, has not been met at 40 mm. The decreased vigor of the rupture between 20 and 40 mm may be due to viscoelastic effects.

[62] This example highlights the fact that the ruptures produced in the experiments are not steady; their tip speeds and slip velocity profiles evolve as they propagate along the interface. This is natural for such a nonlinear and dynamic problem as rupture propagation. Such variability in time and space is characteristic of real earthquakes, as illustrated by earthquake inversions. In several cases, experimental measurements at the 40 mm location result in smaller maximum slip velocity than those at the 20 mm location (e.g., Figure 5). The decrease could be due to the 3-D effect as discussed in

section 3.3 or viscoelastic properties of Homalite. In some cases, particularly pulse-like cases, this may also be an indication of a decaying rupture. Note that decaying ruptures are a very interesting common case to study, since most earthquakes remain relatively small, producing the well-known Gutenberg-Richter distribution of sizes. In all cases, the ruptures produced in the experiments are healthy enough to propagate all the way to the edges of the sample, covering distances much larger than the nucleation region (although we plot results only within a smaller time window that excludes reflections from the boundaries). This indicates that the produced ruptures, even if decaying, are clearly self-driven (or spontaneous).

[63] Figure 17 shows that the majority of experiments have produced supershear ruptures. We see that higher inclination angles and higher compressive loads promote supershear transition. This is consistent with prior theoretical and numerical studies [Andrews, 1976; Xia et al., 2004; Lu et al., 2009]. The black dotted line that separates the supershear and sub-Rayleigh regions is generated based on the analysis of the supershear transition by Andrews [1976] and Lu et al. [2007]. Andrews [1976] considered an in-plane 2-D shear rupture on an interface governed by linear slip-weakening friction, in which the shear strength of the interface decreases linearly from its static value  $\tau_s$  to its dynamic values  $\tau_d$  over the critical slip  $D_c$ , and then remains at  $\tau_d$  during subsequent sliding. Using this model, he demonstrated that the transition distance depends only on

the critical crack half-length  $L_c$  and on the seismic ratio  $s$  as follows:

$$L = F(s)L_c, L_c = \frac{\mu(\tau_s - \tau_d)D_c}{\pi(1 - \nu)(\tau_0 - \tau_d)^2}, s = \frac{\tau_s - \tau_0}{\tau_0 - \tau_d}. \quad (7)$$

$F(s)$  is a numerically determined function that can be approximated by  $F(s) = 9.8(1.77 - s)^{-3}$  as discussed by *Rosakis et al.* [2007]. The parameters  $\mu$  and  $\nu$  are the shear modulus and Poisson's ratio of the elastic solid and  $\tau_0$  is the initial shear stress acting on the interface. For the geometry of our experiment, the transition distance can be expressed as [*Rosakis et al.*, 2007]

$$L = F(s) \frac{\mu(f_s - f_d)D_c}{\pi(1 - \nu)(\sin \alpha - f_d \cos \alpha)^2 P}, s = \frac{f_s - \tan \alpha}{\tan \alpha - f_d}, \quad (8)$$

where  $f_s = \tau_s/\sigma_0$  and  $f_d = \tau_d/\sigma_0$  are the static and dynamic friction coefficients, respectively. The numerical studies of *Lu et al.* [2007] demonstrate that the dynamic nature of the rupture initiation procedure reduces the transition distances by 30% to 40%. To compare the theoretical prediction of the separation between sub-Rayleigh and supershear ruptures to the results of our experiments, we (1) use values  $f_s = 0.6$ ,  $f_d = 0.2$ , and  $D_c = 13 \mu\text{m}$ , as these values enabled the numerical simulations of *Lu et al.* [2009] to match the experimentally determined transition distances of *Xia et al.* [2004], (2) calculate the values of the transition distance  $L$  using the above formula for ranges of experimental parameters represented in Figure 17, (3) apply the reduction factor of 33% motivated by the study of *Lu et al.* [2007], and (4) plot the line corresponding to transition distances of 60 mm (black dotted line in Figure 17). Making the theoretical boundary between sub-Rayleigh and supershear ruptures correspond to the transition distance of 60 mm is consistent with the size of our observation window which is 60 mm in radius. From Figure 17, the resulting boundary is consistent with the experimental results. The line is quite successful in putting experimentally observed supershear ruptures into the same region. It also predicts the extent of the sub-Rayleigh region, which can be more fully explored in future experimental studies.

## 9. Conclusions

[64] We have experimentally observed a systematic increase in the risetime (i.e., local rupture duration) with both (1) increasing nondimensional shear prestress and (2) increasing absolute levels of shear and normal prestress for the same value of the nondimensional shear prestress. Our results confirm the findings of *Lu et al.* [2007] that pulse-like ruptures can exist in the absence of a bimaterial effect or local heterogeneities. We interpret the increase in the risetime as the variation of rupture mode from pulse-like to crack-like. The systematic increase in the risetime and the associated systematic variation of rupture modes presented in this work are qualitatively consistent with the theoretical study of velocity-weakening interfaces by *Zheng and Rice* [1998]. In fact, the experimental study on the variation of rupture mode due to different absolute levels of stress, achieved in the experimental setup by varying the far-field

compression  $P$ , has been motivated by the analyses of *Zheng and Rice* [1998] and *Lu et al.* [2007].

[65] To ensure that the sliding is not driven by fault-normal stress decrease (and the corresponding decrease in frictional resistance) propagating along the interface due to the rupture nucleation procedure, we have conducted fault-normal velocity measurements. The measurements are quite challenging due to the minute relative displacements involved, which are about two orders of magnitude smaller than the fault-parallel displacements. Our results indicate that there is no fault-normal stress reduction at the location which is used to infer the rupture mode. Furthermore, changing the intensity of the explosion in the range that still initiates dynamic rupture does not affect the local rupture duration and hence the rupture mode. That is why velocity-weakening friction remains the most viable explanation for the variation in rupture modes observed in our experiments.

[66] Both pulse-like and crack-like rupture modes can propagate with sub-Rayleigh and supershear rupture speeds. All four potential rupture types (sub-Rayleigh pulse-like, supershear pulse-like, sub-Rayleigh crack-like, and supershear crack-like) are observed in our experiments. The resulting supershear rupture speeds for the two modes are consistent with the analytical predictions of the velocity-weakening model of *Samudrala et al.* [2002]. The observed boundaries, in terms of the experimental parameters, of the pulse-like versus crack-like rupture modes and sub-Rayleigh versus supershear rupture speeds, are well-described by the theory of *Zheng and Rice* [1998] and the supershear transition criterion based on the work of *Andrews* [1976] as developed for our experimental setup [*Xia et al.*, 2004; *Lu et al.*, 2009].

[67] The agreement between our experimental observations and models of velocity-weakening faults suggests that velocity-weakening friction plays an important role in dynamic behavior of ruptures and implies that expressing dynamic weakening of friction solely in terms of slip may not be a sufficiently general description. Our preliminary numerical simulations [*Lu*, 2008; *Lu et al.*, 2010] show that linear slip-weakening friction, which is often used in single-rupture earthquake studies, fails to produce pulse-like modes in a numerical model that represents our experiments, despite the fact that the chosen friction parameters were shown to reproduce the experimentally observed supershear transition distances by *Lu et al.* [2009]. For a range of parameters that results in pulse-like ruptures in the experiments, the simulations with linear slip-weakening friction produce rapidly dying ruptures that do not reach the locations of velocimeter measurements [*Lu*, 2008; *Lu et al.*, 2010]. Simulations that incorporate rate and state friction laws with enhanced velocity weakening at seismic slip rates, with the steady state dependence as in equation (4), do produce pulse-like ruptures, although our preliminary simulation attempts have had difficulty in reproducing the full range of experimental observations. This is likely because we do not know the precise high-velocity friction properties of the experimental interface. Obtaining an independent measurement of such properties would be an important validation of the conclusions of this work. To reproduce the experimental results in a convincing numerical model, we also need to quantify the temporal and spatial parameters of the initiation procedure. Even though the initiation proce-

ture does not seem to decrease the normal stress outside of the nucleation region, it can still affect rupture propagation. Further experimental and theoretical studies are needed to fully quantify those effects.

[68] In our experiments, pulse-like modes correspond to the levels of nondimensional shear prestress significantly lower than the static friction coefficient. If pulse-like ruptures prevail on natural faults, at least for large earthquakes, our study implies that faults operate at low levels of prestress compared to their static strength. This is consistent with the conclusions reached by several theoretical and numerical studies [Rice, 1994; Lapusta and Rice, 2004; Rice, 2006; Noda et al., 2009].

[69] **Acknowledgments.** Nadia Lapusta gratefully acknowledges the support of NSF grant EAR 0548277 for this study. Ares J. Rosakis also gratefully acknowledges the support of NSF grants EAR 0207873 and EAR 0911723, the U.S. Department of Energy grant DE-FG52-06NA 26209, and MURI grant N000140610730 (Y.D.S. Rajapakse, Program Manager).

## References

- Andrews, D. J. (1976), Rupture velocity of plane strain shear cracks, *J. Geophys. Res.*, *81*, 5679–5687, doi:10.1029/JB081i032p05679.
- Andrews, D. J., and Y. Ben-Zion (1997), Wrinkle-like slip pulse on a fault between different materials, *J. Geophys. Res.*, *102*, 553–571, doi:10.1029/96JB02856.
- Beeler, N. M., and T. E. Tullis (1996), Self-healing slip pulses in dynamic rupture models due to velocity-dependent strength, *Bull. Seismol. Soc. Am.*, *86*(4), 1130–1148.
- Ben-Zion, Y. (2001), Dynamic ruptures in recent models of earthquake faults, *J. Mech. Phys. Solids*, *49*(9), 2209–2244, doi:10.1016/S0022-5096(01)00036-9.
- Beroza, G. C., and T. Mikumo (1996), Short slip duration in dynamic rupture in the presence of heterogeneous fault properties, *J. Geophys. Res.*, *101*, 22,449–22,460, doi:10.1029/96JB02291.
- Burridge, R. (1973), Admissible speeds for plane-strain self-similar shear cracks with friction but lacking cohesion, *Geophys. J. R. Astron. Soc.*, *35*, 439–455.
- Cochard, A. D. L., and R. Madariaga (1994), Dynamic faulting under rate-dependent friction, *Pure Appl. Geophys.*, *142*(3–4), 419–445, doi:10.1007/BF00876049.
- Cochard, A., and R. Madariaga (1996), Complexity of seismicity due to highly rate-dependent friction, *J. Geophys. Res.*, *101*, 25,321–25,336, doi:10.1029/96JB02095.
- Cochard, A., and J. R. Rice (2000), Fault rupture between dissimilar materials: Ill-posedness, regularization, and slip-pulse response, *J. Geophys. Res.*, *105*, 25,891–25,907, doi:10.1029/2000JB900230.
- Dally, J. W., and W. F. Riley (1991), *Experimental Stress Analysis*, McGraw-Hill, New York.
- Day, S. M. (1982), Three-dimensional finite difference simulation of fault dynamics: Rectangular faults with fixed rupture velocity, *Bull. Seismol. Soc. Am.*, *72*(3), 705–727.
- Day, S. M., G. Yu, and D. J. Wald (1998), Dynamic stress changes during earthquake rupture, *Bull. Seismol. Soc. Am.*, *88*(2), 512–522.
- Dieterich, J. H. (1979), Modeling of rock friction: 1. Experimental results and constitutive equations, *J. Geophys. Res.*, *84*, 2161–2168, doi:10.1029/JB084iB05p02161.
- Dieterich, J. H. (1981), Constitutive properties of faults with simulated gouge, in *Mechanical Behavior of Crustal Rocks*, *Geophys. Monogr. Ser.*, vol. 24, edited by N. L. Carter et al., pp. 103–120, AGU, Washington, D. C.
- Dieterich, J. H., and B. D. Kilgore (1994), Direct observation of frictional contacts—new insights for state-dependent properties, *Pure Appl. Geophys.*, *143*(1–3), 283–302, doi:10.1007/BF00874332.
- Dieterich, J. H., and B. D. Kilgore (1996), Imaging surface contacts: Power law contact distributions and contact stresses in quartz, calcite, glass and acrylic plastic, *Tectonophysics*, *256*(1–4), 219–239, doi:10.1016/0040-1951(95)00165-4.
- Di Toro, G., D. L. Goldsby, and T. E. Tullis (2004), Friction falls towards zero in quartz rock as slip velocity approaches seismic rates, *Nature*, *427*(6973), 436–439, doi:10.1038/nature02249.
- Festa, G., and J. P. Vilotte (2006), Influence of the rupture initiation on the intersonic transition: Crack-like versus pulse-like modes, *Geophys. Res. Lett.*, *33*, L15320, doi:10.1029/2006GL026378.
- Heaton, T. H. (1990), Evidence for and implications of self-healing pulses of slip in earthquake rupture, *Phys. Earth Planet. Inter.*, *64*(1), 1–20, doi:10.1016/0031-9201(90)90002-F.
- Ida, Y. (1972), Cohesive force across the tip of a longitudinal-shear crack and Griffith's specific surface energy, *J. Geophys. Res.*, *77*, 3796–3805, doi:10.1029/JB077i020p03796.
- Johnson, E. (1992), The influence of the lithospheric thickness on bilateral slip, *Geophys. J. Int.*, *108*(1), 151–160, doi:10.1111/j.1365-246X.1992.tb00846.x.
- Kanamori, H., and D. L. Anderson (1975), Theoretical basis of some empirical relations in seismology, *Bull. Seismol. Soc. Am.*, *65*(5), 1073–1095.
- Kostrov, B. V. (1966), Unsteady propagation of longitudinal shear cracks, *J. Appl. Math. Mech.*, *30*(6), 1241–1248, doi:10.1016/0021-8928(66)90087-6.
- Lapusta, N., and J. R. Rice (2004), Earthquake sequences on rate and state faults with strong dynamic weakening, *Eos Trans. AGU*, *85*(47), Fall Meet. Suppl., Abstract T22A-05.
- Lapusta, N., J. R. Rice, Y. Ben-Zion, and G. Zheng (2000), Elastodynamic analysis for slow tectonic loading with spontaneous rupture episodes on faults with rate- and state-dependent friction, *J. Geophys. Res.*, *105*, 23,765–23,789, doi:10.1029/2000JB900250.
- Liu, Y., and N. Lapusta (2008), Transition of mode II cracks from sub-Rayleigh to intersonic speeds in the presence of favorable heterogeneity, *J. Mech. Phys. Solids*, *56*(1), 25–50, doi:10.1016/j.jmps.2007.06.005.
- Lu, X. (2008), Combined experimental and numerical study of spontaneous rupture on frictional interfaces, Ph.D. thesis, Graduate Aero. Lab., Calif. Inst. of Technol., Pasadena Calif.
- Lu, X., N. Lapusta, and A. J. Rosakis (2007), Pulse-like and crack-like ruptures in experiments mimicking crustal earthquakes, *Proc. Natl. Acad. Sci. U. S. A.*, *104*, 18,931–18,936, doi:10.1073/pnas.0704268104.
- Lu, X., N. Lapusta, and A. J. Rosakis (2009), Analysis of supershear transition regimes in rupture experiments: The effect of nucleation conditions and friction parameters, *Geophys. J. Int.*, *177*(2), 717–732, doi:10.1111/j.1365-246X.2009.04091.x.
- Lu, X., N. Lapusta, and A. J. Rosakis (2010), Pulse-like and crack-like dynamic shear ruptures on frictional interfaces: Experimental evidence, numerical modeling, and implications, *Int. J. Fract.*, *163*, 27–39, doi:10.1007/s10704-010-9479-4.
- Lykotrafitis, G. (2006a), Experimental study of dynamic frictional sliding modes along incoherent interfaces, Ph.D. thesis, Graduate Aero. Lab., Calif. Inst. of Technol., Pasadena, Calif.
- Lykotrafitis, G., A. J. Rosakis, and G. Ravichandran (2006b), Self-healing pulse-like shear ruptures in the laboratory, *Science*, *313*(5794), 1765–1768, doi:10.1126/science.1128359.
- Lykotrafitis, G., A. J. Rosakis, and G. Ravichandran (2006c), Particle velocimetry and photoelasticity applied to the study of dynamic sliding along frictionally-held bimaterial interfaces: Techniques and feasibility, *Exp. Mech.*, *46*(2), 205–216, doi:10.1007/s11340-006-6418-4.
- Madariaga, R. (1976), Dynamics of an expanding circular fault, *Bull. Seismol. Soc. Am.*, *66*(3), 639–666.
- Nielsen, S., and R. Madariaga (2003), On the self-healing fracture mode, *Bull. Seismol. Soc. Am.*, *93*(6), 2375–2388, doi:10.1785/0120020090.
- Nielsen, S. B., J. M. Carlson, and K. B. Olsen (2000), Influence of friction and fault geometry on earthquake rupture, *J. Geophys. Res.*, *105*, 6069–6088, doi:10.1029/1999JB900350.
- Noda, H., E. M. Dunham, and J. R. Rice (2009), Earthquake ruptures with thermal weakening and the operation of major faults at low overall stress levels, *J. Geophys. Res.*, *114*, B07302, doi:10.1029/2008JB006143.
- Olsen, K. B., R. Madariaga, and R. J. Archuleta (1997), Three-dimensional dynamic simulation of the 1992 Landers Earthquake, *Science*, *278*(5339), 834–838, doi:10.1126/science.278.5339.834.
- Perrin, G., J. R. Rice, and G. Zheng (1995), Self-healing slip pulse on a frictional surface, *J. Mech. Phys. Solids*, *43*(9), 1461–1495, doi:10.1016/0022-5096(95)00036-1.
- Rice, J. R. (1994), Earthquakes at low driving stress in a high strength, low toughness fault zone: Shear-heating example, *Eos Trans. AGU*, *75*(44), Fall Meet. Suppl., F426.
- Rice, J. R. (2006), Heating and weakening of faults during earthquake slip, *J. Geophys. Res.*, *111*, B05311, doi:10.1029/2005JB004006.
- Rosakis, A. J. (2002), Inter-sonic shear cracks and fault ruptures, *Adv. Phys.*, *51*, 1189–1257, doi:10.1080/00018730210122328.
- Rosakis, A. J., K. W. Xia, G. Lykotrafitis, and H. Kanamori (2007), Earthquake seismology dynamic shear rupture in frictional interfaces: Speeds, directionality and modes, in *Treatise in Geophysics*, vol. 4, pp. 153–192, edited by G. Schubert and H. Kanamori, Elsevier, Amsterdam.

- Ruina, A. (1983), Slip instability and state variable friction laws, *J. Geophys. Res.*, *88*, 10,359–10,370, doi:10.1029/JB088iB12p10359.
- Samudrala, O., Y. Huang, and A. J. Rosakis (2002), Subsonic and intersonic shear rupture of weak planes with a velocity weakening cohesive zone, *J. Geophys. Res.*, *107*(B8), 2170, doi:10.1029/2001JB000460.
- Shi, Z. Q., and Y. Ben-Zion (2006), Dynamic rupture on a bimaterial interface governed by slip-weakening friction, *Geophys. J. Int.*, *165*(2), 469–484, doi:10.1111/j.1365-246X.2006.02853.x.
- Shi, Z., Y. Ben-Zion, and A. Needleman (2008), Properties of dynamic rupture and energy partition in a solid with a frictional interface, *J. Mech. Phys. Solids*, *56*(1), 5–24, doi:10.1016/j.jmps.2007.04.006.
- Tsutsumi, A., and T. Shimamoto (1997), High-velocity frictional properties of gabbro, *Geophys. Res. Lett.*, *24*, 699–702, doi:10.1029/97GL00503.
- Tullis, T. E., and D. L. Goldsby (2003), Flash melting of crustal rocks at almost seismic slip rates, *Eos Trans. AGU*, *84*(46), Fall Meet. Suppl., Abstract S51B-05.
- Xia, K. W., A. J. Rosakis, and H. Kanamori (2004), Laboratory earthquakes: The sub-Rayleigh-to-supershear rupture transition, *Science*, *303*, 1859–1861, doi:10.1126/science.1094022.
- Yuan, F., and V. Prakash (2008a), Slip weakening in rocks and analog materials at coseismic slip rates, *J. Mech. Phys. Solids*, *56*(2), 542–560, doi:10.1016/j.jmps.2007.05.007.
- Yuan, F., and V. Prakash (2008b), Use of a modified torsional Kolsky bar to study frictional slip resistance in rock-analog materials at coseismic slip rates, *Int. J. Solids Struct.*, *45*(14–15), 4247–4263, doi:10.1016/j.ijsolstr.2008.03.012.
- Zheng, G., and J. R. Rice (1998), Conditions under which velocity-weakening friction allows a self-healing versus a cracklike mode of rupture, *Bull. Seismol. Soc. Am.*, *88*, 1466–1483.

---

N. Lapusta, Division of Engineering and Applied Science, California Institute of Technology, Pasadena, CA 91125, USA. (lapusta@its.caltech.edu)  
 X. Lu and A. J. Rosakis, Graduate Aerospace Laboratories, California Institute of Technology, Pasadena, CA 91125, USA. (xiaolu.galcit@gmail.com; rosakis@aero.caltech.edu)